Neutrinos from STORed Muons
Letter of Intent

P. Kyberd and D.R. Smith
Brunel University

L. Coney
University of California, Riverside

S. Pascoli
Institute for Particle Physics Phenomenology, Durham University

C. Ankenbrandt, S.J. Brice, A.D. Bross, H. Cease, J. Kopp,
N. Mokhov, D. Neuffer, M. Popovic, P. Rubinov, and S. Striganov
Fermi National Accelerator Laboratory

A. Blondel, A. Bravar, and E. Noah
University of Geneva

R. Bayes and P. Soler
University of Glasgow

A. Dobbs, K. Long, J. Pasternak, E. Santos, and M.O. Wascko
Imperial College London

S.K. Agarwalla
Instituto de Fisica Corpuscular, CSIC and Universidad de Valencia

S.A. Bogacz
Jefferson Laboratory

Y. Mori and J.B. Lagrange
Kyoto University

A. de Gouvêa
Northwestern University

Y. Kuno and A. Sato
Osaka University

V. Blackmore, J. Cobb, and C. D. Tunnell
Oxford University, Subdepartment of Particle Physics

W. Winter
Institut für theoretische Physik und Astrophysik, Universität Würzburg

CONTENTS

I. OVERVIEW

The idea of using a muon storage ring to produce a high-energy ($\simeq$ 50 GeV) neutrino beam for experiments was first discussed by Koshkarev [1] in 1974. A detailed description of a muon storage ring for neutrino oscillation experiments was first produced by Neuffer [2] in 1980. In his paper, Neuffer studied muon decay rings with E_μ of 8, 4.5 and 1.5 GeV. With his 4.5 GeV ring design, he achieved a figure of merit of $\simeq 6 \times 10^9$ useful neutrinos per 3×10^{13} protons on target. The facility we describe here (νSTORM) is essentially the same facility proposed in 1980 and would utilize a 3-4 GeV/c muon storage ring to study eV-scale oscillation physics and, in addition, could add significantly to our understanding of ν_e and ν_μ cross sections. In particular the facility can:

1. address the large Δm^2 oscillation regime and make a major contribution to the study of sterile neutrinos,
2. make precision ν_e and $\bar{\nu}_e$ cross-section measurements,
3. provide a technology (μ decay ring) test demonstration and μ beam diagnostics test bed,
4. provide a precisely understood ν beam for detector studies.

The facility is the simplest implementation of the Neutrino Factory concept [3]. In our case, 60 GeV/c protons are used to produce pions off a conventional solid target. The pions are collected with a focusing device (horn or lithium lens) and are then transported to, and injected into, a storage ring. The pions that decay in the first straight of the ring can yield a muon that is captured in the ring. The circulating muons then subsequently decay into electrons and neutrinos. We are starting with a storage ring design that is optimized for 3.8 GeV/c muon momentum. This momentum was selected to maximize the physics reach for both oscillation and the cross section physics. See Fig. 1 for a schematic of the facility.

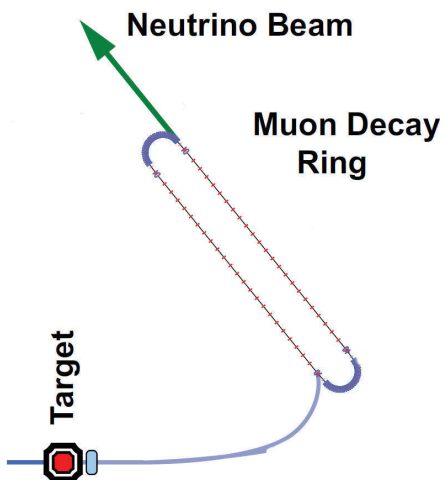

Figure 1. Schematic of the facility

It would also be possible to create a $\pi \rightarrow \mu$ decay channel and inject the muons into the decay ring with a kicker magnet. This scheme would have the advantage that the transport channel could be longer than the straight in the decay ring and thus allow for more π decays to result in a useful μ. This does complicate the facility design, however, due to the need for the kicker magnet and the desire to use single-turn extraction from the Main Injector.

Muon decay yields a neutrino beam of precisely known flavor content and energy. For example for positive muons: $\mu^+ \rightarrow e^+ + \bar{\nu}_\mu + \nu_e$. In addition, if the circulating muon flux in the ring is measured accurately (with beam-current transformers, for example) then the neutrino beam flux is also accurately known. Near and far detectors are placed along the line of one of the straight sections of the racetrack decay ring. The near detector can be placed at 20-50 meters from the end of the straight. A near detector for disappearance measurements will be identical to the far detector, but only about one tenth the fiducial mass. It will require a μ catcher, however. Additional purpose-specific near detectors can also be located in the near hall and will measure neutrino-nucleon cross sections. νSTORM can provide the first precision measurements of ν_e and $\bar{\nu}_e$ cross sections which are important for future long-baseline experiments. A far detector at $\simeq$ 1000 m would study neutrino oscillation physics and would be capable of performing searches in both appearance and disappearance channels. The experiment will take advantage of the "golden channel" of oscillation appearance $\nu_e \rightarrow \nu_\mu$, where the resulting final state has a muon of the wrong-sign from interactions of the $\bar{\nu}_\mu$ in the beam. In the case of μ^+s stored in the ring, this would mean the observation of an event with a μ^-. This detector would need to be magnetized for the wrong-sign muon appearance channel, as is the case for the current baseline Neutrino Factory detector [4]. A number of possibilities for the far detector exist. However, a magnetized iron detector similar to that used in MINOS is likely to be the most straight forward approach for the far detector design that meets the performance requirements to reach our physics goals. For the purposes of the νSTORM oscillation physics, a detector inspired by MINOS, but with thinner plates and much larger excitation current (larger B field) is assumed.

II. THEORETICAL AND EXPERIMENTAL MOTIVATIONS

A. Sterile neutrinos in extensions of the Standard Model

Sterile neutrinos, fermions that are uncharged under the $SU(3) \times SU(2) \times U(1)$ gauge group, arise naturally in many extensions to the Standard Model. Even where they are not an integral part of a model, they can usually be easily accommodated. A detailed overview of the phenomenology of sterile neutrinos and of related model building considerations is given in [5].

For instance, in Grand Unified Theories (GUTs), fermions are grouped into multiplets of a large gauge group, of which $SU(3) \times SU(2) \times U(1)$ is a subgroup. If these multiplets

contain not only the known quarks and leptons, but also additional fermions, these new fermions will, after the breaking of the GUT symmetry, often behave like gauge singlets (see for instance [6–9] for GUT models with sterile neutrinos).

Models attempting to explain the smallness of neutrino masses through a seesaw mechanism generically contain sterile neutrinos. While in the most generic seesaw scenarios, these sterile neutrinos are extremely heavy ($\sim 10^{14}$ GeV) and have very small mixing angles ($\sim 10^{-12}$) with the active neutrinos, slightly non-minimal seesaw models can easily feature sterile neutrinos with eV-scale masses and with percent level mixing with the active neutrinos. Examples for non-minimal seesaw models with relatively light sterile neutrinos include the split seesaw scenario [10], seesaw models with additional flavor symmetries (see e.g. [11]), models with a Froggatt-Nielsen mechanism [12, 13], and extended seesaw models that augment the mechanism by introducing more than three singlet fermions, as well as additional symmetries [14–16].

Furthermore, sterile neutrinos arise naturally in "mirror models", in which the existence of an extended "dark sector", with nontrivial dynamics of its own, is postulated. If the dark sector is similar to the visible sector, as is the case, for instance, in string-inspired $E_8 \times E_8$ models, it is natural to assume that it also contains neutrinos [17–19].

Finally, sterile neutrinos also have an impact in cosmology on the evolution of the Early Universe and on astrophysical objects such as supernovae (for a review see [5] and references therein). By mixing with active neutrinos, they can be produced in the Early Universe by oscillations before neutrino decoupling. They could constitute the dark matter (DM) of the Universe, if they have masses in the keV range, or part of it in the case of lighter masses in the eV range, in which case they contribute to hot DM. A thermal population of a light sterile neutrino acts as an additional relativistic degree of freedom at sufficiently high temperatures. If present, they affect Big Bang Nucleosynthesis, the Cosmic Microwave Background (CMB) and the formation of large scale structures such as galaxies and clusters of galaxies. Their effect on the CMB anisotropies is due mainly to the change of the matter radiation equality redshift and the sound horizon at the time of CMB decoupling and to their anisotropic stress which suppresses the amplitude of higher harmonics in the temperature anisotropy spectrum. Interestingly, recent observations of the CMB by WMAP and of the CMB damping tail by ACT and SPT indicate a value of the effective number of relativistic degrees of freedom higher than 3 at a significant confidence level, suggesting the existence of sterile neutrinos or of a thermal population of other light particles, in addition to 3 active neutrinos. If future observations, and in particular Planck, confirm this result, testing the mixing angles required for a thermal distribution of sterile neutrinos to be produced in the Early Universe will be of paramount importance in order to establish the identity of the additional relativistic degrees of freedom in the Universe. νSTORM could test a large part of the required parameter space, having sensitivity to the relevant masses and mixing angles with different flavors.

B. Experimental hints for light sterile neutrinos

While the theoretical motivation for the existence of sterile neutrinos is certainly strong, what has mostly prompted the interest of the scientific community in this topic are several experimental results that show significant deviations from the Standard Model predictions. These results can be interpreted as hints for oscillations involving sterile neutrinos.

The first of these hints was obtained by the LSND collaboration, who carried out a search for $\bar{\nu}_\mu \to \bar{\nu}_e$ oscillations over a baseline of $\sim$ 30 m [20]. Neutrinos were produced in a stopped pion source in the decay $\pi^+ \to \mu^+ + \nu_\mu$ and the subsequent decay $\mu^+ \to e^+ \bar{\nu}_\mu \nu_e$. Electron antineutrinos are detected through the inverse beta decay reaction $\bar{\nu}_e p \to e^+ n$ in a liquid scintillator detector. Backgrounds to this search arise from the decay chain $\pi^- \to \bar{\nu}_\mu + (\mu^- \to \nu_\mu \bar{\nu}_e e^-)$ if negative pions produced in the target decay before they are captured by a nucleus, and from the reaction $\bar{\nu}_\mu p \to \mu^+ n$, which is only allowed for the small fraction of muon antineutrinos produced by pion decay *in flight* rather than stopped pion decay. The LSND collaboration finds an excess of $\bar{\nu}_e$ candidate events above this background with a significance of more than 3σ. When interpreted as $\bar{\nu}_\mu \to \bar{\nu}_e$ oscillations through an intermediate sterile state $\bar{\nu}_s$, this result is best explained by sterile neutrinos with an effective mass squared splitting $\Delta m^2 \gtrsim 0.2$ eV^2 relative to the active neutrinos, and with an effective sterile-induced $\bar{\nu}_\mu$–$\bar{\nu}_e$ mixing angle $\sin^2 2\theta_{e\mu,\text{eff}} \gtrsim 2 \times 10^{-3}$, depending on Δm^2.

The MiniBooNE experiment [21, 22] was designed to test the neutrino oscillation interpretation of the LSND result using a different technique, namely neutrinos from a horn-focused pion beam. While a MiniBooNE search for $\nu_\mu \to \nu_e$ oscillations indeed disfavors most (but not all) of the parameter region preferred by LSND in the simplest model with only one sterile neutrino [21], the experiment obtains results *consistent* with LSND when running in antineutrino mode and searching for $\bar{\nu}_\mu \to \bar{\nu}_e$. Due to low statistics, however, the antineutrino data favors LSND-like oscillations over the null hypothesis only at the 90% confidence level. Moreover, MiniBooNE observes a yet unexplained 3.0σ excess of ν_e-like events (and, with smaller significance also of $\bar{\nu}_e$ events) at low energies, 200 MeV $\lesssim E_\nu \lesssim$ 475 MeV, outside the energy range where LSND-like oscillations would be expected.

A third hint for the possible existence of sterile neutrinos is provided by the so-called reactor antineutrino anomaly. In 2011, Mueller *et al.* published a new *ab initio* computation of the expected neutrino fluxes from nuclear reactors [23]. Their results improve upon a 1985 calculation by Schreckenbach [24] by using up-to-date nuclear databases, a careful treatment of systematic uncertainties and various other corrections and improvements that were neglected in the earlier calculation. Mueller *et al.* find that the predicted antineutrino flux from a nuclear reactor is about 3% higher than previously thought. This result, which was later confirmed by Huber [25], implies that short baseline reactor experiments have observed a 3σ *deficit* of antineutrinos compared to the prediction [5, 26]. It needs to be emphasized that the significance of the deficit depends crucially on the systematic uncertainties associated with the theoretical prediction, some of which are difficult to estimate reliably. If the reactor antineutrino deficit is interpreted as $\bar{\nu}_e \to \bar{\nu}_s$ disappearance via oscillation, the required 2-flavor oscillation parameters are $\Delta m^2 \gtrsim 1$ eV^2 and $\sin^2 2\theta_{ee,\text{eff}} \sim 0.1$.

Such short-baseline oscillations could also explain another experimental result: the Gallium anomaly. The GALLEX and SAGE solar neutrino experiments used electron neutrinos from intense artificial radioactive sources to test their radiochemical detection principle [27–31]. Both experiments observed fewer ν_e from the source than expected. The statistical significance of the deficit is above 99% and can be interpreted in terms of short-baseline $\bar{\nu}_e \to \bar{\nu}_s$ disappearance with $\Delta m^2 \gtrsim 1$ eV^2 and $\sin^2 2\theta_{ee,\text{eff}} \sim 0.1$–$0.8$. [32–34].

C. Constraints and global fit

While the previous section shows that there is an intriguing accumulation of hints for the existence of new oscillation effects—possibly related to sterile neutrinos—in short-baseline experiments, these hints are not undisputed. Several short-baseline oscillation experiments did *not* confirm the observations from LSND, MiniBooNE, reactor experiments, and Gallium experiments, and place very strong limits on the relevant regions of parameter space in sterile neutrino models. To assess the viability of these models it is necessary to carry out a global fit to all relevant experimental data sets, and several groups have endeavored to do so [5, 35–39]. In Fig. II C [5, 35], we show the current constraints on the parameter space of a $3+1$ model (a model with three active neutrinos and one sterile neutrino). We have projected the parameter space onto a plane spanned by the mass squared difference Δm^2 between the heavy, mostly sterile mass eigenstate and the light, most active ones and by the effective amplitude $\sin^2 2\theta_{e\mu,\text{eff}}$ for $\nu_\mu \to \nu_e$ 2-flavor oscillations to which LSND and MiniBooNE are sensitive.

We see that there is severe tension in the global data set: the parameter region favored by LSND and MiniBooNE antineutrino data is disfavored at more than 99% confidence level by searches for ν_e ($\bar{\nu}_e$) and $\bar{\nu}_\mu$ disappearance. Using a parameter goodness-of-fit test [59] to quantify this tension, p-values on the order of few $\times 10^{-6}$ are found for the compatibility of LSND and MiniBooNe $\bar{\nu}$ data with the rest of the global data set, and p-values smaller than 10^{-3} are found for the compatibility of appearance data and disappearance data [5]. The global fit improves somewhat in models with more than one sterile neutrino, but significant tension remains [5, 35].

One can imagine several possible resolutions to this puzzle:

1. One or several of the apparent deviations from the standard three neutrino oscillation framework discussed in section II B have explanations not related to sterile neutrinos.
2. One or several of the null results that favor the no-oscillation hypothesis are in error.
3. There are more than two sterile neutrino flavors. Note that scenarios with one sterile neutrino with an eV scale mass are already in some tension with cosmology, even though the existence of one sterile neutrino with a mass well below 1 eV is actually preferred by cosmological fits [60–63]. Cosmological bounds on sterile neutrinos can be avoided in non-standard cosmologies [64] or by invoking mechanisms that suppress sterile neutrino production in the early universe [65, 66].

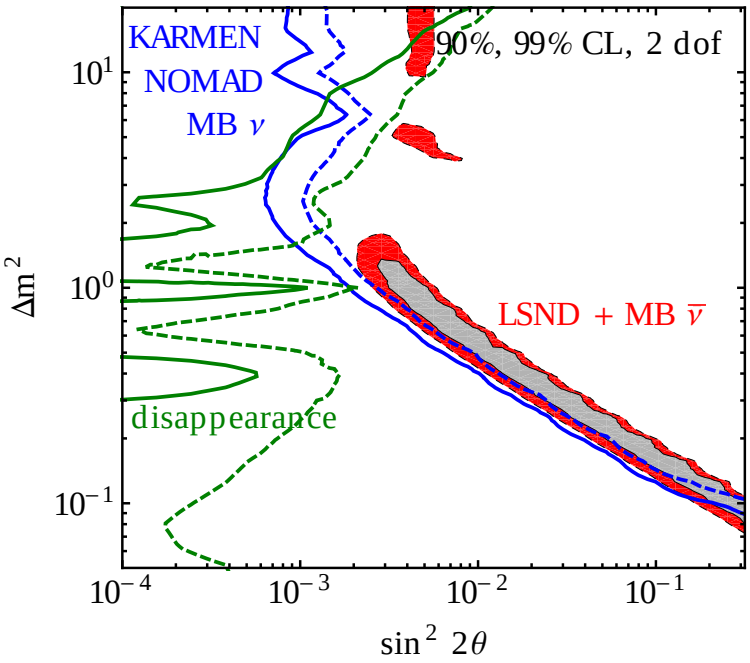

Figure 2. Global constraints on sterile neutrinos in a 3+1 model. We show the allowed regions at 90% and 99% CL from a combined analysis of the LSND [20] and MiniBooNE antineutrino [22] signals (filled regions), as well as the constraints from the null results of KARMEN [40], NOMAD [41] and MiniBooNE neutrino [21] appearance searches (blue contour). The limit from disappearance experiments (green contours) includes data from CDHS [42], atmospheric neutrinos [43], MINOS [44, 45], and from SBL reactor experiments [46–53]. For the latter, we have used the new reactor flux predictions from [23], but we have checked that the results, especially regarding consistency with LSND and MiniBooNE $\bar{\nu}$ data, are qualitatively unchanged when the old reactor fluxes are used. Fits have been carried out in the GLoBES framework [54, 55] using external modules discussed in [56–58]

4. There are sterile neutrinos plus some other kind of new physics at the eV scale. (See for instance [58, 67] for an attempt in this direction.)

We conclude that our understanding of short baseline neutrino oscillations is currently incomplete. On the one hand, several experiments indicate deviations from the established three-neutrino framework. However, none of these hints can be considered conclusive, and moreover, when interpreted in the simplest sterile neutrino models, they are in severe tension with existing constraints on the parameter space of these models. An experiment searching for short-baseline neutrino oscillations with good sensitivity and well-controlled systematic uncertainties has great potential to clarify the situation by either finding a new type of neutrino oscillation or by deriving a strong and robust constraint on any such oscillation. The requirements for this proposed experiment are as follows:

- Direct test of the LSND and MiniBooNE anomalies.
- Provide stringent constraints for both ν_e and ν_μ disappearance to overconstrain $3+N$ oscillation models and to test the Gallium and reactor anomalies directly.
- Test the CP- and T-conjugated channels as well, in order to obtain the relevant clues for the underlying physics model, such as CP violation in $3+2$ models.

Neutrino production with a muon storage ring is the only option which can fulfill these requirements simultaneously, since both ν_e ($\bar{\nu}_e$) and $\bar{\nu}_\mu$ (ν_μ) are in the beam in equal quantities.

D. Measurement of neutrino-nucleon scattering cross sections

A number of recent articles have presented detailed reviews of the status of neutrino-nucleon scattering cross section measurements in the context of the oscillation-physics programme (see for example [68] and references therein). The effect of uncertainties in the neutrino scattering cross sections is to reduce the sensitivity of the present and future short- and long-baseline experiments. The impact of the uncertainties on the cross sections is particularly pernicious at large θ_{13}. This is illustrated in figure 3 where the sensitivity of the T2HK experiment to CP-invariance violation is plotted as a function of $\sin^2 2\theta_{13}$ [69]. The experiment considered in this analysis assumes a proton beam power of 4 MW is used to generate a conventional super-beam illuminating a 500 kT water Cherenkov detector at a distance of 295 km from the source. The analysis assumes a 0.1kT water Cherenkov near detector at a distance of 2 km. Figure 3 shows that, for $\theta_{13} \sim 0.1$, the statistical power of the experiment can only be exploited if the neutrino scattering cross sections times efficiencies are known with a precision of $\sim 1\%$ and the ratio of the electron-neutrino cross section times efficiency to the muon-neutrino cross section times efficiency is known to $\sim 1\%$. Experiments that exploit a wide-band neutrino beam with a near/far detector combination that is capable of resolving the first and second oscillation maxima are less severely affected by the cross section errors. However, the sensitivity of such experiments to CP-invariance violation is significantly enhanced if it is assumed that the cross sections have been determined with a precision of 1% or better [70].

The search for the existence of sterile neutrinos through the measurement of oscillations requires that an anomalous rate of electron-neutrino appearance, or muon-neutrino disappearance, be demonstrated. This requires that accurate predictions can be made of the neutrino event rates that would be expected in the absence of active/sterile neutrino mixing. The experiment described in this LOI is conceived to rule out, at the level of at least 5σ, the hypothesis that the anomalies observed in the LSND, MiniBOONE, MINOS and reactor experiments may be attributed to statistical fluctuations or unexpected background processes. To do this requires that the neutrino-nucleon scattering cross sections are measured accurately.

Figure 4 shows the present data on the charged-current neutrino-scattering cross sections in the relevant energy range. The neutrino flux that will be generated by the 3.8 GeV stored

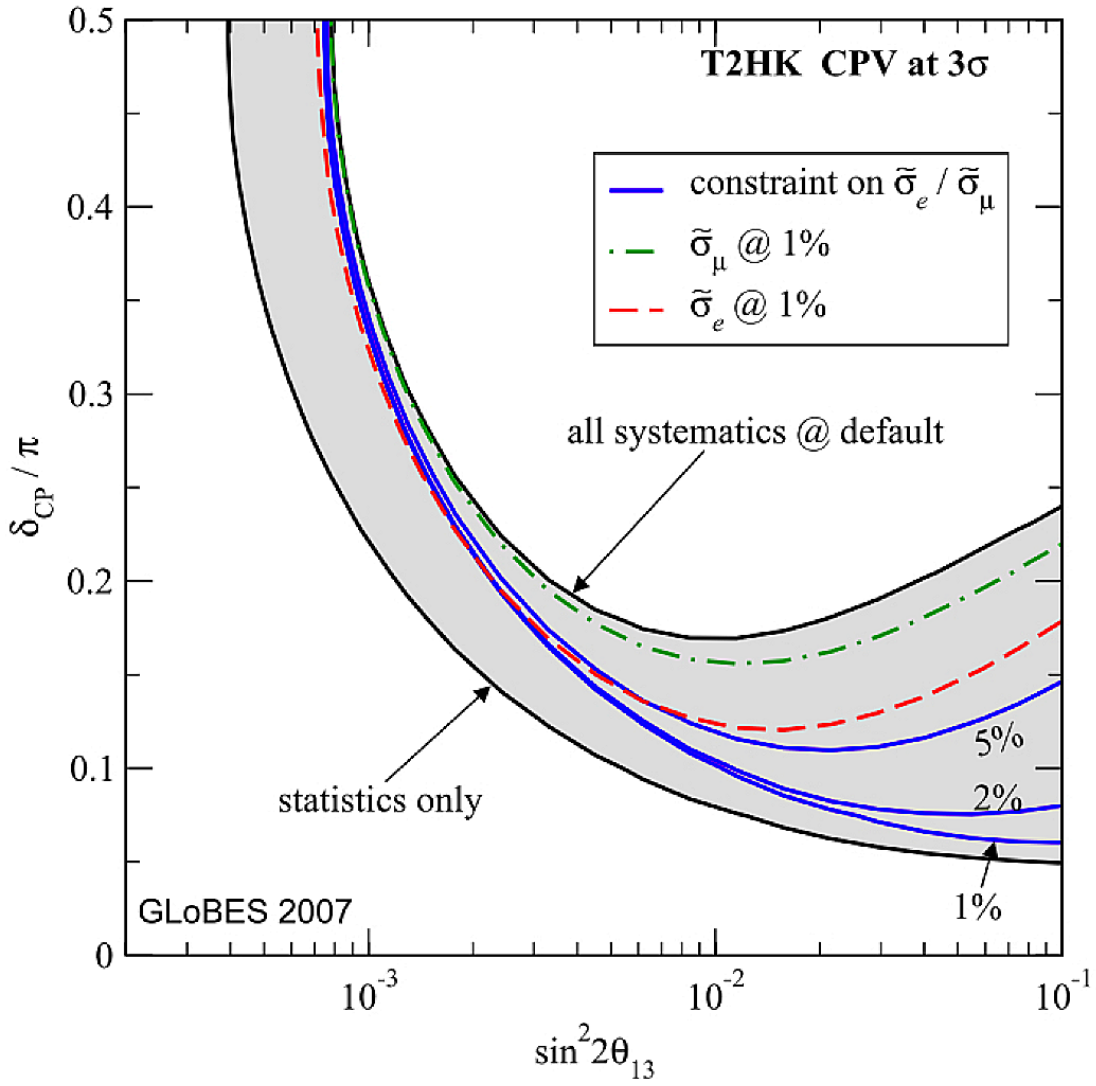

Figure 3. T2HK sensitivity to CP-invariance violation at 3σ. The sensitivity that would be obtained in the absense of systematic uncertainties is shown by the lower solid black line. Taking systematic errors into account, as described in [69] yields the sensitivity shown by the upper solid black line. The sensitivity that would pertain if the product of the efficiency and the (anti)neutrino scattering cross sections (denoted $\bar{\sigma}_{\mu,e}$ are known with a precision of 1% are shown by the dashed red, and dot dashed green lines. The solid blue lines show the effect of an uncertainty of 1%, 2% and 5% on the ratio of the electron- to muon-neutrino times the relevant efficitiency. Figure taken from [69].

muon beam proposed here will allow cross section measurements in the neutrino-energy range $1-3\,\mathrm{GeV}$, the region in which the $\nu_\mu N$ data shown in figure 4 is sparse. Moreover, ν_e appearance searches rely on $\nu_e N$ cross sections for which there is essentially no data. At present, estimates of the electron-neutrino cross sections are made by extrapolation of the muon neutrino cross sections. Such extrapolations suffer from substantial uncertainties arising from non-perturbative hadronic corrections and it is therefore essential that detailed measurements of the $\nu_e N$ and $\nu_\mu N$ scattering cross sections and hadron-production rates

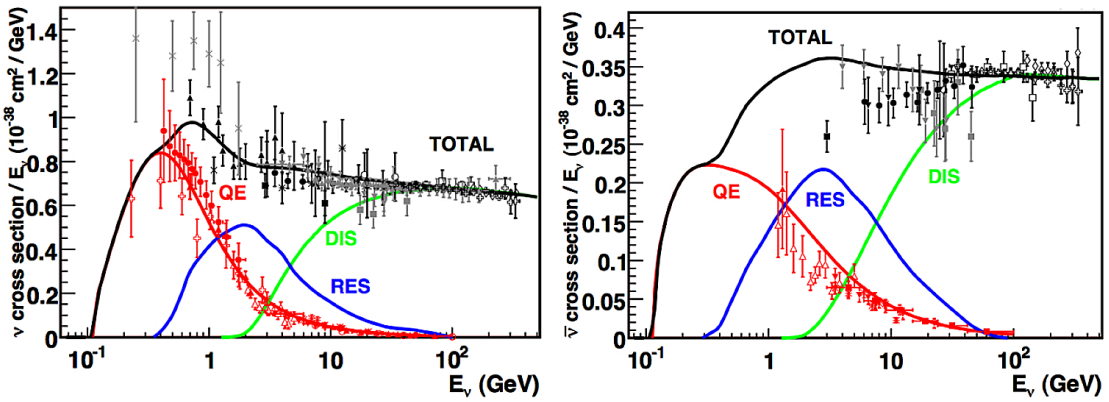

Figure 4. The neutrino-nucleon (left panel) and antineutrino-nucleon (right panel) cross sections plotted asa a function of (anti)neutrino energy [71]. The data are compared to the expectations of the models described in [72]. The processes that contribute to the total cross section (shown by the black lines) are: quasi-elastic (QE, red lines) scattering; resonance procuction (RES, blue lines); and deep inelastic scattering (DIS, green lines). The uncertainties in the energy range of interest are typically $10-40\%$. Figure taken from [68].

are performed. The νSTORM facility, therefore, has a unique opportunity. The flavour composition of the beam and the neutrino energy spectrum are both known precisely. In addition, the storage ring instrumentation combined with measurements at the near detector will allow the neutrino flux to be measured with a precision of 1%. Substantial event rates may be obtained in a fine-grained detector placed between 20 m and 50 m from the storage ring. Therefore, the objective is to measure the $\nu_e N$ and $\nu_\mu N$ scattering cross sections for neutrino energies in the range $1-3$ GeV with a precision approaching 1%. This will be a critical contribution to the search for sterile neutrinos and will be of fundamental importance to the present and next generation of long-baseline neutrino oscillation experiments.

III. FACILITY

The basic concept for the facility is presented in Fig. 1. A high-intensity proton source places beam on a target, producing a large spectrum of secondary pions. Forward pions are focused by a collection element into a transport channel. Pions decay within the first straight of the decay ring and a fraction of the resulting muons are stored in the ring. Muon decay within the straight sections will produce ν beams of known flux and flavor via: $\mu^+ \to e^+ + \bar{\nu}_\mu + \nu_e$ or $\mu^- \to e^- + \nu_\mu + \bar{\nu}_e$. For the implementation which is described here, we choose a 3.8 GeV/c storage ring to obtain the desired spectrum of $\simeq 2$ GeV neutrinos (see Fig. 42). This means that we must capture pions at a momentum of approximately 5 GeV/c.

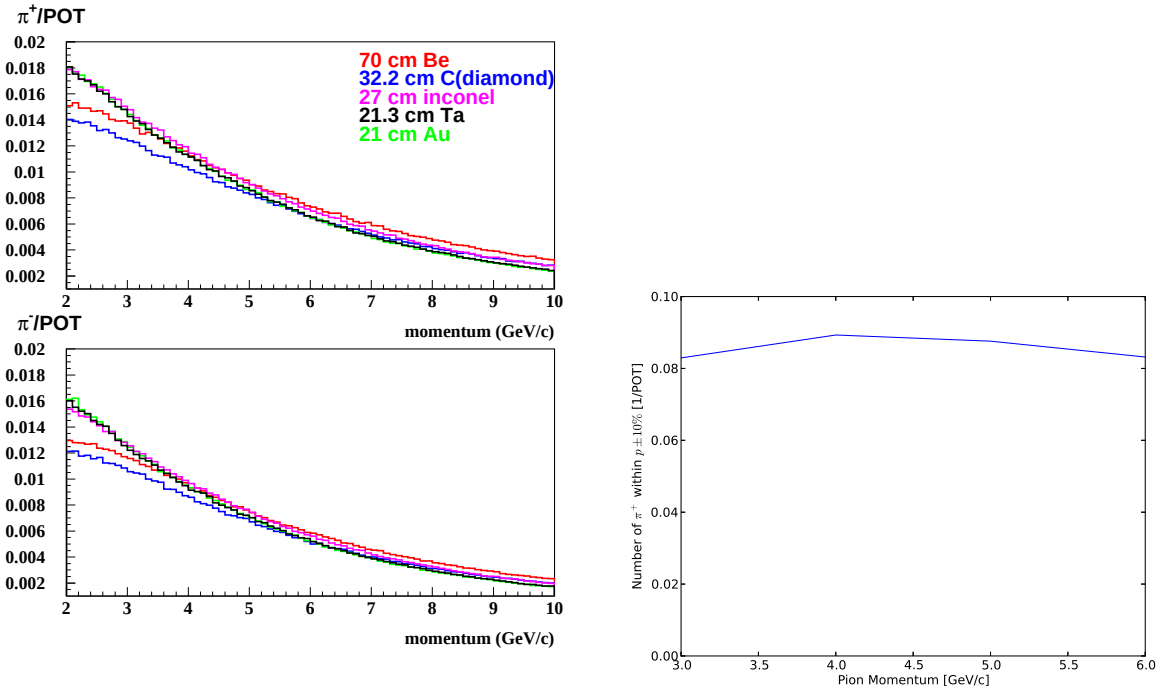

Figure 5. Left: π production off various targets into a forward cone of 120 mrad per 100 MeV bin. Upper π^+, lower π^-. Right: Integrated Production for the case of 70 cm Be target.

A. Targeting and capture

The number of pions produced off various targets by 60 GeV/c protons has been simulated with the MARS code [73]. The results of this analysis on a number of different targets are shown in Fig. 5 (left) where the number in a foward cone of 120 mrad per proton on target as a function of energy is given.

In Fig. 5 (left) we see that the pion production decreases monotonically with increasing momentum. Fig. 5 (right) shows number of pions produced off a 70 cm Be target as a function of energy where a linear interpolation is used to integrate π(p) in $\pm$10% momentum bins and we see that that yield is relatively flat in energy. Since the integration range is relative (the range increases with increasing momentum), this compensates for the monotonic decrease shown in Fig. 5 (left).

We have also performed a target optimization based on a conservative estimate for the decay-ring acceptance of 2 mm-radian. This corresponds to a decay ring with 11 cm internal radius and a β function of 600 cm. Measurements of positive pion production at 70 GeV [74, 75] are in $\sim$ 30% agreement with MARS predictions for production of pions in the momentum range of 3-5 GeV/c and at small angles. It is well known that the maximum yield can be achieved with a target radius of $\sim 3\times$ the proton beam RMS size . The optimal target length depends on the target material and the secondary pion momentum. Results of the optimization study are presented in Table I. We see that approximately 0.11 π^+/POT

Table I. π^+ yield/POT at 60 GeV/c into 2 mm radian acceptance.

material	momentum (GeV/c)	±15%	±10%	±5%	target length (cm)	density (g/cm^3)
Carbon	3	0.085	0.056	0.028	27.3	3.52
Carbon	5	0.099	0.067	0.033	32.2	3.52
Inconel	3	0.131	0.087	0.044	19.2	8.43
Inconel	5	0.136	0.091	0.045	27.0	8.43
Tantalum	3	0.164	0.109	0.054	15.3	16.6
Tantalum	5	0.161	0.107	0.053	21.3	16.6
Gold	3	0.177	0.118	0.059	18.0	19.32
Gold	5	0.171	0.112	0.056	21.0	19.32

can be collected into a ± 10% momentum acceptance off medium/heavy targets assuming ideal capture.

Regarding capture/collection, we have looked into two options, a lithium lens and a horn. The existing Fermilab lithium lens has a working gradient of 2.6 tesla/cm at 15 Hz. The optimal distance between the target and lens center is about 25 cm. Pions produced into a 2 mm-radian acceptance have a wide radial distribution, however. Fig. 6 (Left) shows the π radial distribution 5 cm downstream of the target. The current Fermilab lens with its 1 cm radius would capture only 40% of the pions in a ± 10% momentum bin. With a 2 cm lens, the transmission factor increases up to 60%. Further improvement could be achieved by increasing the lens gradient, but increasing the gradient reduces the focal length. Maximal transmission could reach 80% with a 4 Tesla/m gradient and a 2 cm lens radius. But this is beyond the current state-of-the-art for an operating lens and the target downstream end would then need to be very close to the lens. With a NuMI-like horn operating at 300 kA and using a 22 cm gold target, it is possible to collect 0.088 π^+/POT within a momentum band of 5 ± 0.5 GeV/c. The β function of the pion beam after the horn is about 200 cm in this case. Note that shape of the NuMI horn inner conductor was chosen to maximize the yield of neutrinos with energy $\leq$ 12 GeV. Optimization of the horn inner shape could increase the number of collected pions. The spatial distribution of the pions just downstream of the horn is given in Fig. 6 (Right).

For our muon flux calculations we use a 20% loss of pions during the collection phase (from the 0.88 above and the numbers in Table I for gold, 5 GeV/c and ± 10% capture. The transport efficiency is assumed to be ~ 1 and the injection efficiency is assumed to be 90%.

B. Injection options

An obvious goal for the facility is to collect as many pions as possible (within the limits of available beam power), inject them into the decay ring and capture as many muons as possible from the $\pi \to \mu$ decays. With pion decay within the ring, non-Liouvillean "stochastic injection" is possible. In stochastic injection, the $\simeq$ 5 GeV/c pion beam is transported

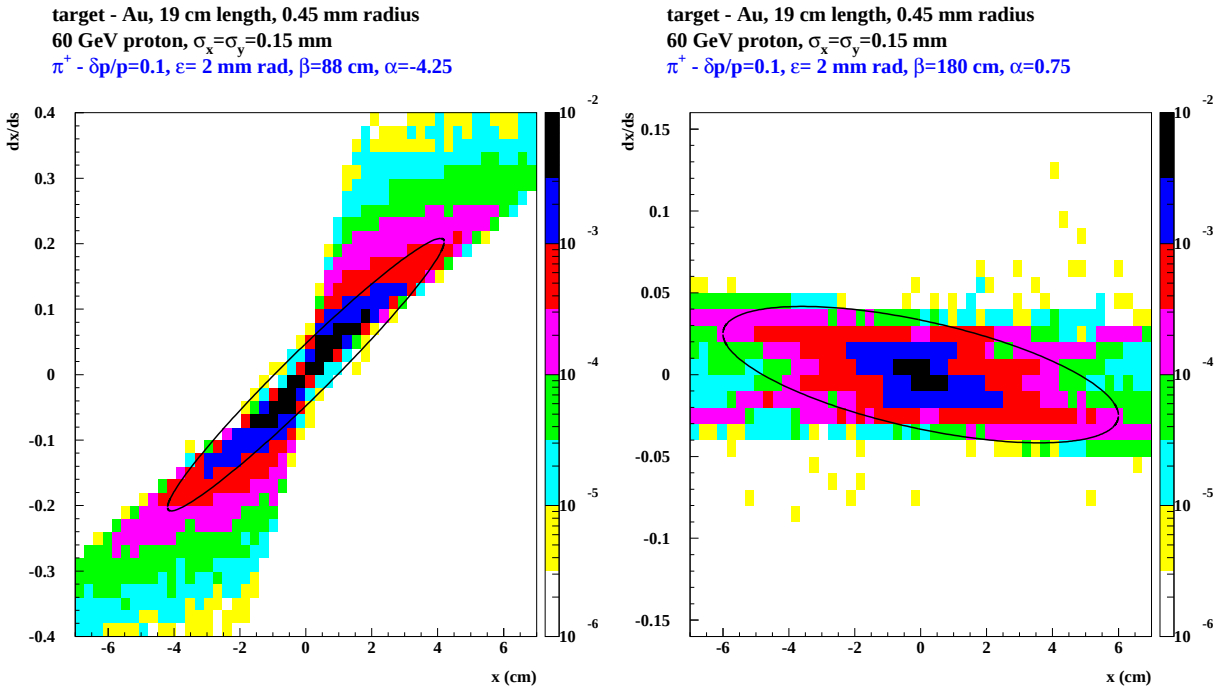

Figure 6. Left: Pion spatial distribution just downstream of the target. Right: Pion spatial distribution just downstream of the horn described above

from the target into the storage ring and dispersion-matched into a long straight section. (Circulating and injection orbits are separated by momentum.) Decays within that straight section provide muons that are within the $\simeq$ 3.8 GeV/c ring momentum acceptance. With stochastic injection, muons from a beam pulse as long as the Main Injector circumference (3000m) can be accumulated, and no injection kickers are needed, see Fig. 7. Note: for 5.0 GeV/c pions, the decay length is $\simeq$ 280m; $\simeq$ 42% decay within the 150m decay ring straight.

As mentioned in section I, decay before injection requires a separate decay transport line and full-aperture fast kickers matching the pion beam pulse to the ring. The decay channel could be based on the conventional FODO channel focused by normal conducting quadrupoles. A preliminary design consisting of 36 cells with the total length of 165.6 m has been done. The quadrupoles are 0.8 m long with the full aperture of about 30 cm and the gradient of 9.7 T/m. The phase advance could be adjusted to provide stable focusing for the full pion momentum range decaying both backward and forward into the useful muon momentum range sets by the final ring acceptance (currently up to $\pm$16%) and to the muon beam being formed simultaneously. The decay channel would need to be followed by a dedicated broad momentum matching section to couple the decay channel with the ring while keeping high transmission. The muon injection into the storage ring requires full-aperture fast kickers and septum magnets, matching the μ beam pulse to the ring. A preliminary considerations suggests that such kickers and the septum can be constructed based on the existing technology, subject to verification in future studies. Developing a

scenario for extraction from the Main Injection would also have to be included in any future studies. At this point (and in the rest of this document), we are assuming pion decay in the ring.

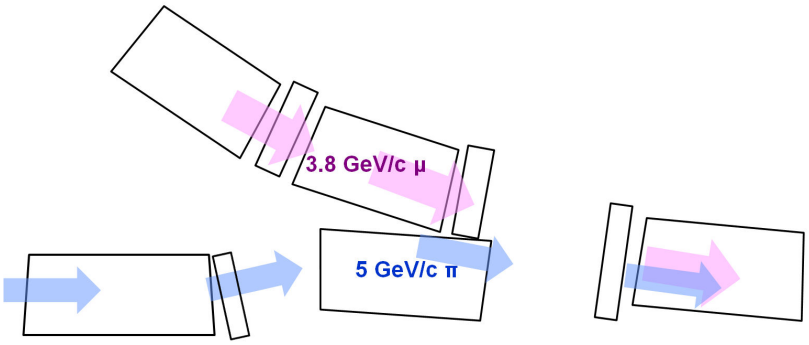

Figure 7. Stochastic injection concept

C. Muon decay ring

We have investigated both a FODO racetrack and a FFAG racetrack for the muon decay. The FODO ring that is described in detail below uses both normal and superconducting magnets. A FODO lattice using only normal-conducting magnets (B $\lesssim$ 2T) is also being developed. In this case, the arcs are twice as long ($\simeq$ 50m), but the straight sections would be similar. The racetrack FFAG (RFFAG) described below uses normal-conducting magnets, but a preliminary investigation with the use of super-ferric magnets for this lattice has been done. In this case, the ring circumference would be reduced from $\sim$ 600m to $\sim$ 450m and the operating costs would be drastically reduced. Table II gives a comparison (at our current level of understanding) between the FODO and the RFFAG with regard to the ratio of the total number of useful muons stored per POT assuming that capture off the target and injection into the rings are the same for both. Acceptance for all the decay ring options we are considering will be studied and compared in order to obtain a cost/performance optimum.

1. Separate element FODO racetrack

Here we propose a compact racetrack ring design based on separate function magnets (bends and quadrupoles only) configured with various flavors of FODO lattice. The ring layout is illustrated in Fig. 8. The design goal for the ring was to maximize both the transverse and momentum acceptance (around 3.8 GeV/c central momentum), while maintaining reasonable physical apertures for the magnets in order to keep the cost down. This was accomplished by employing strongly focusing optics in the arcs (90 deg. phase advance per cell FODO); featuring small β functions ($\simeq$ 3 m average) and low dispersion ($\simeq$ 0.8 m average). The linear optics for one of the 180 deg. arcs is illustrated in Fig. 9. The current FODO lattice

Table II. Relative μ yield for FODO vs. RFFAG rings

Parameter	FODO	RFFAG
$L_{straight}$ (m)	150	240
Circumference (m)	350	606
Dynamic aperture A_{dyn}	0.7	0.95
Momentum acceptance	$\pm$ 10%	$\pm$ 16%
π/POT within momentum acceptance	0.112	0.171
Fraction of π decaying in straight (F_s)	0.41	0.57
Ratio of $L_{straight}$ to ring circumference (Ω)	.43	.40
Relative factor ($A_{dyn} \times \pi$/POT $\times F_s \times \Omega$)	0.014	0.037

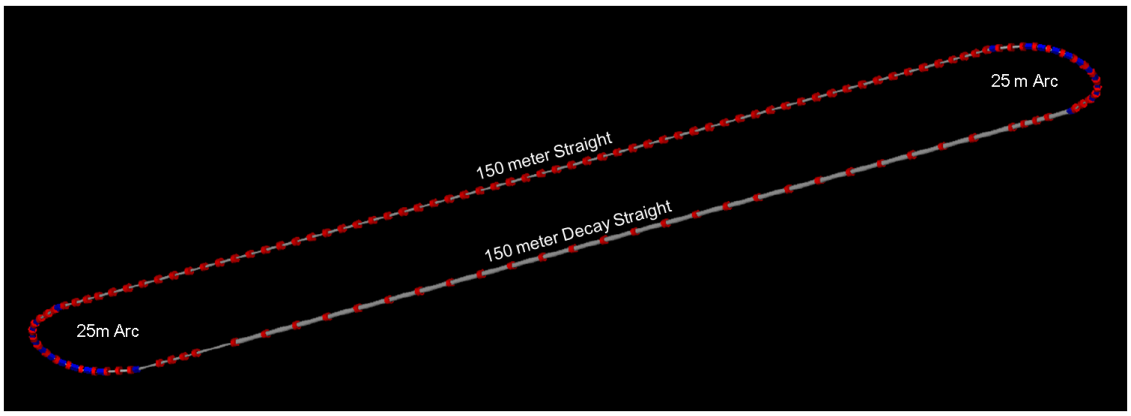

Figure 8. Racetrack ring layout: 150 m straights and 25 m 180 deg. arcs

design incorporates a missing-magnet dispersion suppressor. The missing-magnet dispersion suppressor provides an ideal location for the implementation of stochastic injection, see Fig. 7. With a dispersion of $\eta \simeq 1.2$m at the drift, the 5 and 3.8 GeV/c orbits are separated by $\simeq$ 30 cm; an aperture of $\simeq \pm$ 15cm is available for both the 5 GeV/c π and 3.8 GeV/c μ orbits. To maintain high compactness of the arc, while accommodating adequate drift space for the injection chicane to merge, two special "half empty" cells with only one dipole per cell were inserted at both arc ends to suppress the horizontal dispersion. This solution allowed us to limit the overall arc length to about 25 m, while keeping the dipole fields below 4 Tesla. The arc magnets assume a relatively small physical aperture radius of 15 cm, which limits the maximum field at the quadrupole magnet pole tip to less than 4 Tesla. On the other hand, the decay straight requires much larger values of β functions ($\simeq$ 40 m average)in order to maintain small beam divergence ($\simeq$ 7 mrad). The resulting muon beam divergence is a factor of 4 smaller than the characteristic decay cone of $1/\gamma$ ($\simeq$ 0.028 at 3.8 GeV). As illustrated in Fig. 10, the decay straight is configured with a much weaker focusing FODO lattice (30 deg. phase advance per cell). It uses normal conducting large aperture (r = 30 cm) quads with a modest gradient of 1.1 Tesla/m (0.4 Tesla at the pole tip). Both the arc and the straight are smoothly matched via a compact telescope insert, as illustrated in Fig. 10. The "other" 150 meter straight, which is not used for neutrino production, can

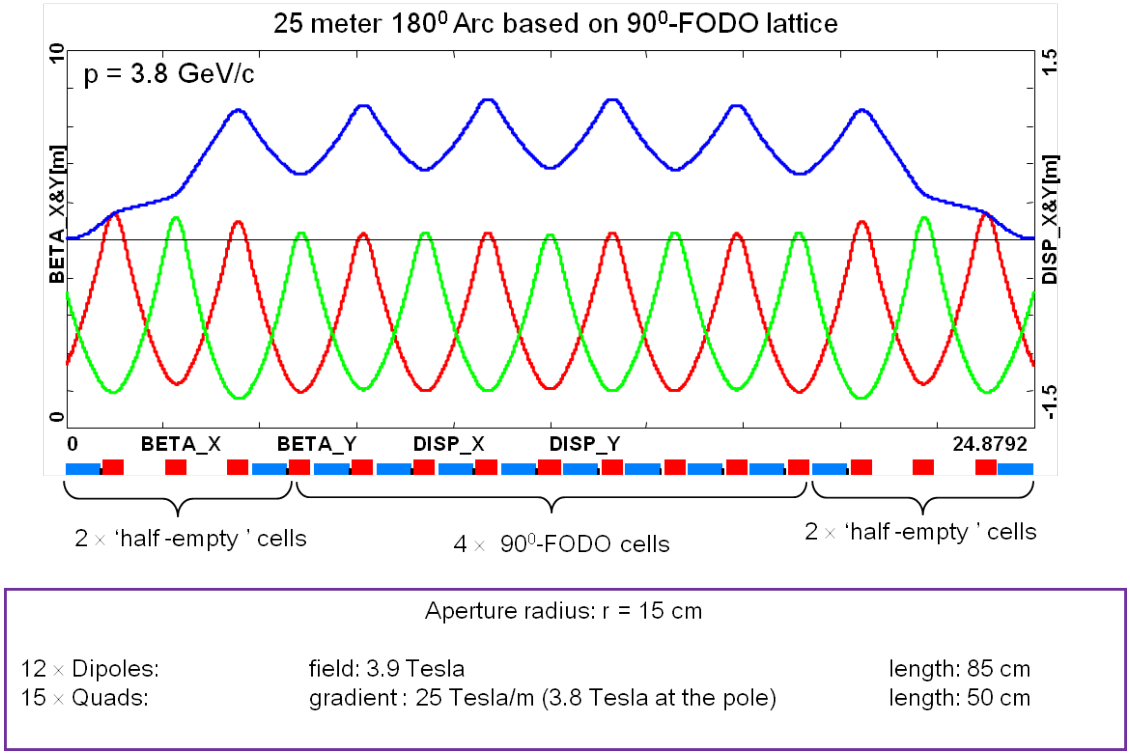

Figure 9. Arc optics with dispersion via missing dipoles with the so called half empty cells; two of them at both arc ends.

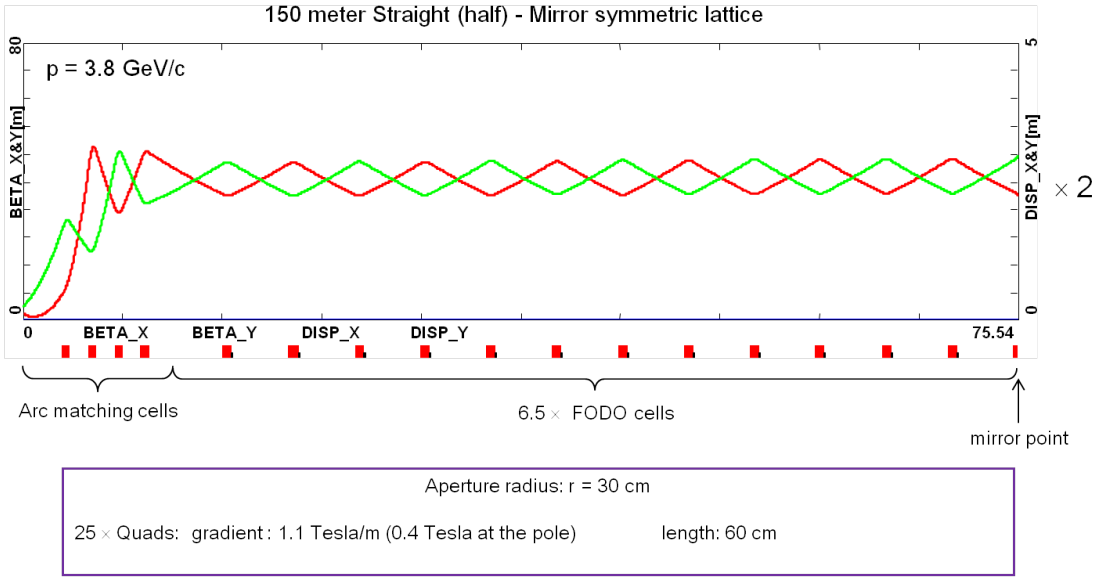

Figure 10. Decay straight optics configured with "high-β" ($\simeq$ 40 m) weakly focusing FODO cells smoothly matched to the arc. Only half of the 150 meter long straight is shown, with the mirror symmetry point indicated on the left end.

be designed using much tighter FODO lattice (60 deg. phase advance per cell), with rather small β functions comparable to the one in the arc ($\simeq$ 5 m average). This way one can restrict the aperture radius of the straight to 15 cm. Again, the second straight uses normal

conducting, quads with a gradient of 11 Tesla/m (1.6 Tesla at the pole tip). Both the arc and the straight are smoothly matched, as illustrated in Fig. 11. Finally, the complete

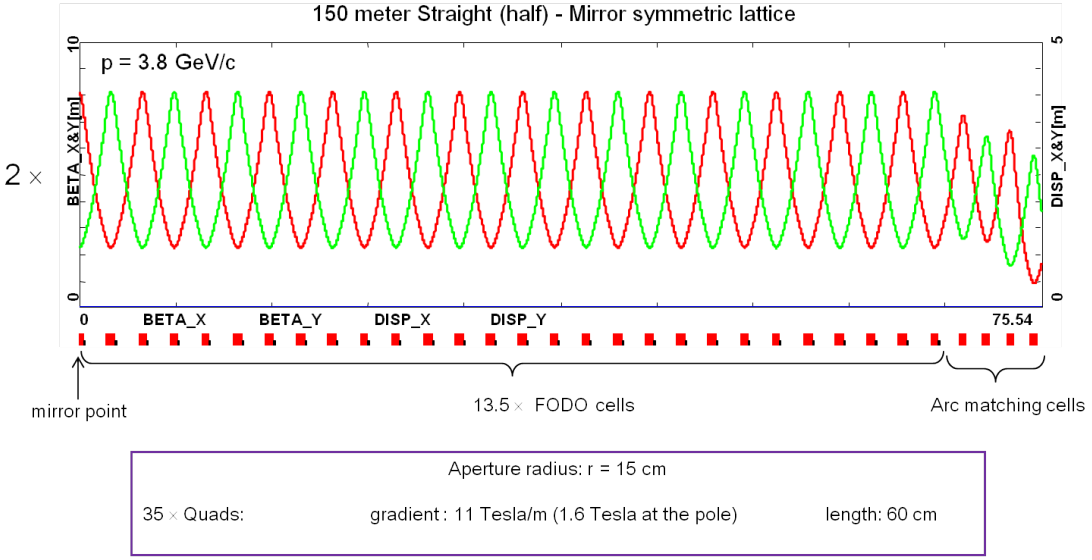

Figure 11. The other straight optics configured with "low-β" ($\simeq$ 5 m) weakly focusing FODO cells smoothly matched to the arc. Only half of the 150 meter long straight is shown, with the mirror symmetry point indicated on the right end.

racetrack ring architecture is illustrated in Fig. 12. It features the "low-β" straight (half) matched to the 180 deg. arc and followed by the "high-β" decay straight (half) connected to the arc with a compact telescope insert. To summarize the magnet requirements, both 180

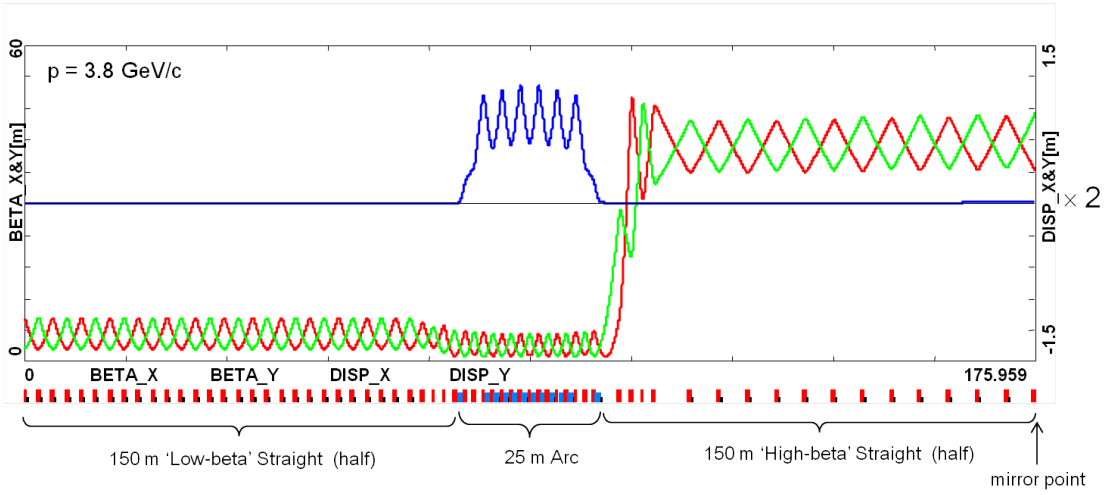

Figure 12. Complete racetrack ring lattice. Only half of the ring is shown, with the mirror symmetry point indicated on the right end.

deg. arcs were configured with 3.9 Tesla dipoles and 25 Tesla/m quads (superconducting magnets with 15 cm aperture radius). Both straights use normal conducting magnets: the decay straight—1.1 Tesla/m quads with 30 cm aperture radius and the other straight —11 Tesla/m quads with 15 cm aperture radius.

The ring acceptance was studied via symplectic tracking (with the OptiM code) of 25,000 muons through 68 turns (e-folding muon decay). The dynamic losses amounted to 30% (70% muons survived 68 turns without accounting for muon decay). The resulting acceptance is summarized in terms of the transverse and longitudinal phase-space projections resulting from multi-particle tracking as illustrated in Fig. 13. In summary, the ring features transverse

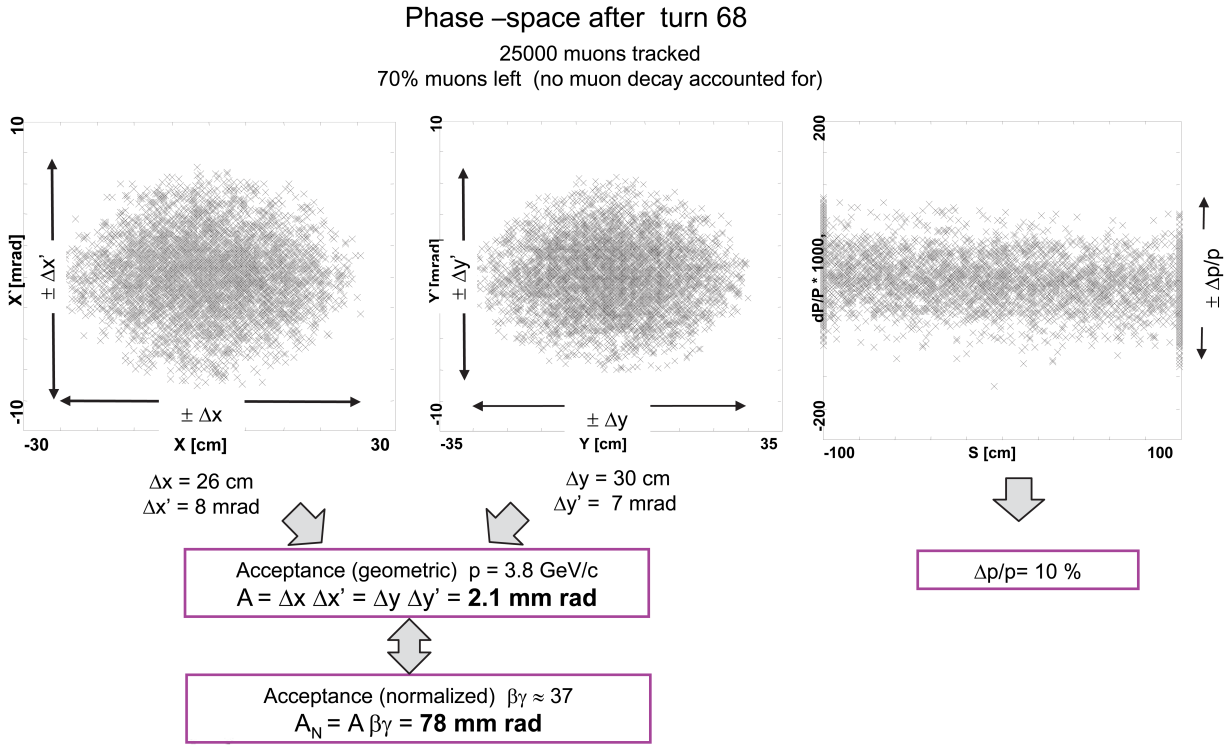

Figure 13. Dynamic aperture study resulting transverse and longitudinal phase-space acceptance after 68 turns of tracking. For illustration, the phase-space snapshots were taken at the middle of the decay straight.

acceptance (normalized) of 78 mm rad both in x and y (or geometric acceptance of 2.1 mm rad) for the net momentum acceptance of ±10%

2. Advanced scaling FFAG

The racetrack FFAG ring is composed of two cell types: a) a straight scaling FFAG cell and b) a circular scaling FFAG cell. There are 40 straight FFAG cells in each long straight section (80 for the whole ring) and 16 circular FFAG cells in each of the arc sections.

a. Straight scaling FFAG cell parameters

In the straight scaling FFAG cell, the vertical magnetic field B_{sz} in the median plane follows:

$$B_{sz} = B_{0sz} e^{m(x-x_0)} \mathcal{F},$$

with x the horizontal Cartesian coordinate, m the normalized field gradient, $\mathcal{F}$ an arbitrary function and $B_{0sz} = B_{sz}(x_0)$. The parameters of the straight scaling FFAG cell are summarized in Table III. The cell is shown in Fig. 14. The red line represents the $\simeq$ 3.8 GeV/c

Cell type		DFD triplet
Number of cells in the ring		80
Cell length		6 m
x_0		36 m
m-value		$2.65\,\mathrm{m}^{-1}$
Packing factor		0.1
Collimators $(x_{min}, x_{max}, z_{max})$		(35.5 m, 36.5 m, 0.3 m)
Periodic cell dispersion		0.38 m
Horizontal phase advance		13.1 deg.
Vertical phase advance		16.7 deg.
D_1 magnet parameters		
	Magnet center	0.2 m
	Magnet length	0.15 m
	Fringe field fall off	Linear (Length: 0.04 m)
	$B_0(x_0 = 36\ m)$	1.28067 T
F magnet parameters		
	Magnet center	3 m
	Magnet length	0.3 m
	Fringe field fall off	Linear (Length: 0.04 m)
	$B_0(x_0 = 36\ m)$	-1.15037 T
D_2 magnet parameters		
	Magnet center	5.8 m
	Magnet length	0.15 m
	Fringe field fall off	Linear (Length: 0.04 m)
	$B_0(x_0 = 36\ m)$	1.28067 T

Table III. Parameters of the straight scaling FFAG cell.

muon reference trajectory, and its corresponding magnetic field is shown in Fig. 15. Periodic β functions are shown in Fig. 16.

b. Circular scaling FFAG cell parameters

In the circular scaling FFAG cell, the vertical magnetic field B_{cz} in the median plane follows

$$B_{cz} = B_{0cz}\left(\frac{r}{r_0}\right)^k \mathcal{F},$$

with r the radius in polar coordinates, k the geometrical field index, $\mathcal{F}$ an arbitrary function and $B_{0cz} = B_{cz}(r_0)$. The parameters of the circular scaling FFAG cell are summarized in Table IV. The cell is shown in Fig. 17. The red line represents the 3.8 GeV/c muon reference trajectory, and its corresponding magnetic field is shown in Fig. 18. Periodic β functions are shown in Fig. 19.

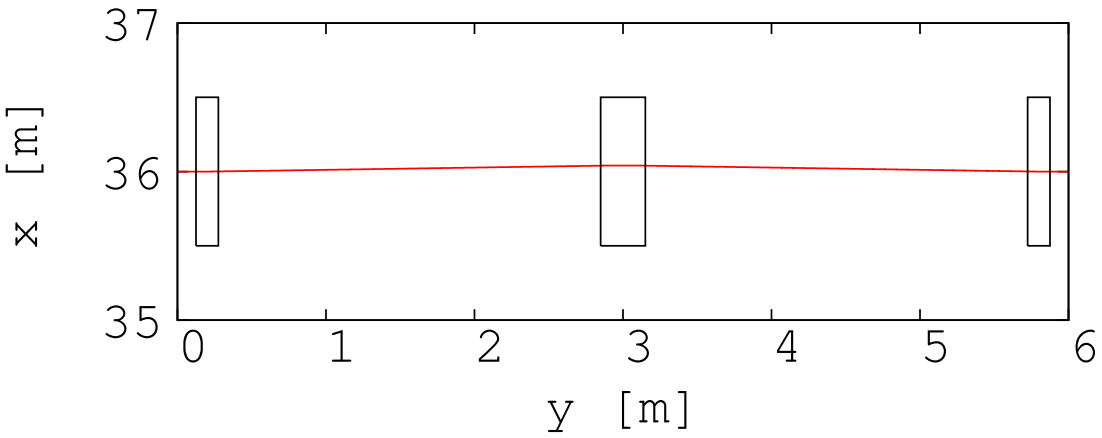

Figure 14. Top view of the straight scaling FFAG cell. The 3.8 GeV/c muon reference trajectory is shown in red. Effective field boundaries with collimators are shown in black.

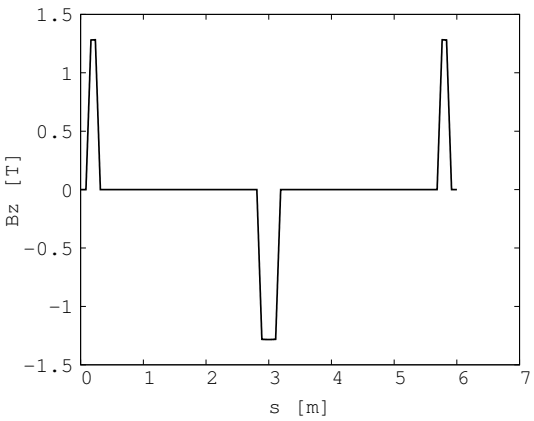

Figure 15. Vertical magnetic field for 3.8 GeV/c muon reference trajectory in the straight scaling FFAG cell.

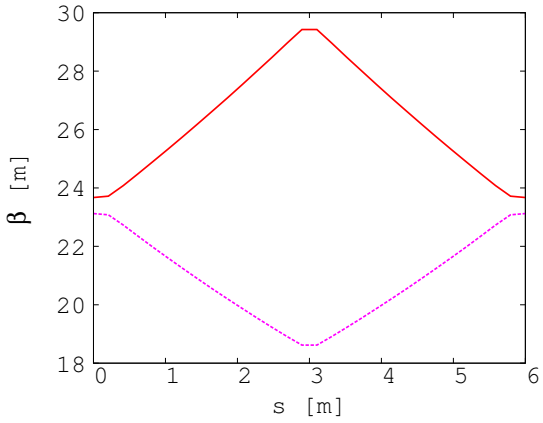

Figure 16. Horizontal (plain red) and vertical (dotted purple) periodic β functions of the straight scaling FFAG cell.

Cell type		FDF triplet
Number of cells in the ring		32
Cell opening angle		11.25 deg
r_0		36 m
k-value		10.85
Packing factor		0.96
Collimators $(r_{min}, r_{max}, z_{max})$		(35 m, 37 m, 0.3 m)
Periodic cell dispersion		1.39 m (at 3.8 GeV/c)
Horizontal phase advance		67.5 deg.
Vertical phase advance		11.25 deg.
F_1 magnet parameters		
	Magnet center	1.85 deg
	Magnet length	3.4 deg
	Fringe field fall off	Linear (Length: 0.1 deg)
	$B_0(r_0 = 36\ m)$	-1.55684 T
D magnet parameters		
	Magnet center	5.625 deg
	Magnet length	4.0 deg
	Fringe field fall off	Linear (Length: 0.1 deg)
	$B_0(r_0 = 36\ m)$	1.91025 T
F_2 magnet parameters		
	Magnet center	9.4 deg
	Magnet length	3.4 deg
	Fringe field fall off	Linear (Length: 0.1 deg)
	$B_0(r_0 = 36\ m)$	-1.55684 T

Table IV. Parameters of the circular scaling FFAG cell.

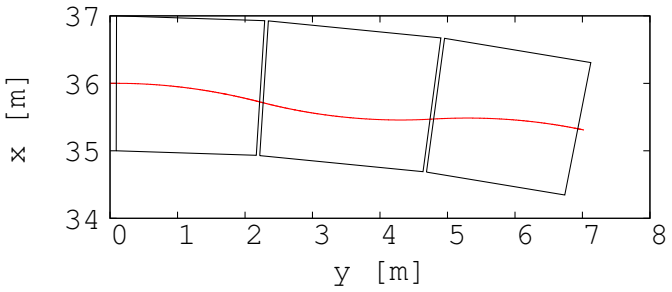

Figure 17. Top view of the circular scaling FFAG cell. The 3.8 GeV/c muon reference trajectory is shown in red. Effective field boundaries with collimators are shown in black.

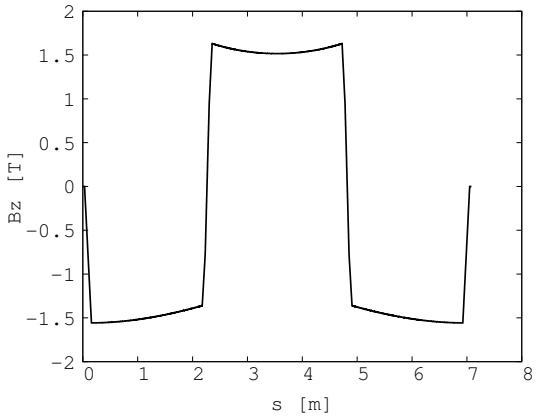

Figure 18. Vertical magnetic field for the 3.8 GeV/c muon reference trajectory in the circular scaling FFAG cell.

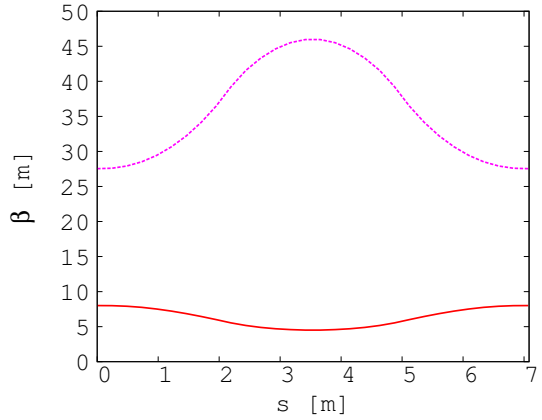

Figure 19. Horizontal (plain red) and vertical (dotted purple) periodic β functions of the circular scaling FFAG cell.

c. Single particle tracking

Stepwise tracking using Runge Kutta integration in a field model with linear fringe fields has been performed where interpolation of the magnetic field away from the mid-plane has been done to first order. Only single particle tracking has been done so far. We used μ^+ with a central momentum, p_0, of 3.8 GeV/c, a minimum momentum, p_{min}, of 3.14 GeV/c and a maximum momentum, p_{max}, of 4.41 GeV/c. $\Delta p/p_0$ is thus $\pm 16\%$. The tracking step size was 1 mm. The exit boundary of a cell is the entrance boundary of the next cell.

The ring tune point is (8.91,4.72) at p_0. Stability of the ring tune has been studied over the momentum range. The tune shift is presented in Fig. 20. The tune point stays within a 0.1 shift.

Closed orbits of p_0, p_{min}, and p_{max} particles are shown in Fig. 21. The magnetic field for the p_{max} closed orbit is presented in Fig. 22. Dispersion at p_0 is shown in Fig. 23. β functions for p_0, p_{min}, and p_{max} are plotted in Fig. 24.

An acceptance study at fixed energy has also been done. The maximum amplitudes with stable motion at p_0 over 30 turns are shown for horizontal and vertical motion in Fig. 25 (left) and in Fig. 26 (right), respectively. The same procedure has been done for p_{min} (see Fig. 27) and p_{max} (see Fig. 29). The results are comparable. The unnormalized maximum emittance is more than 1 mm-radian.

d. Multi-particle tracking

Multi-particle beam tracking in 6-D phase space has been carried out for the beam with $\Delta p/p_0 = \pm 16\%$. Figures 18 and 19 show the results of the beam tracking simulation in the horizontal and vertical directions, respectively. A normalized emittance of 14 mm-radian in the transverse direction is assumed. In these figures, the blue dots show the initial particle

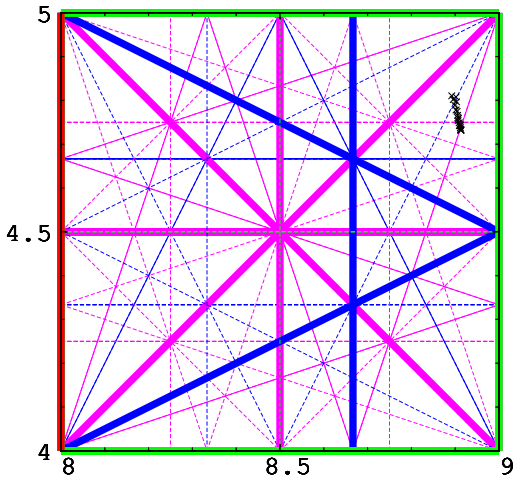

Figure 20. Tune diagram for muons from p_{min} to p_{max} ($\pm 16\%$ in momentum around 3.8 GeV/c). Integer (red), half-integer (green), third integer (blue) and fourth integer (purple) normal resonances are plotted. Structural resonances are in bold.

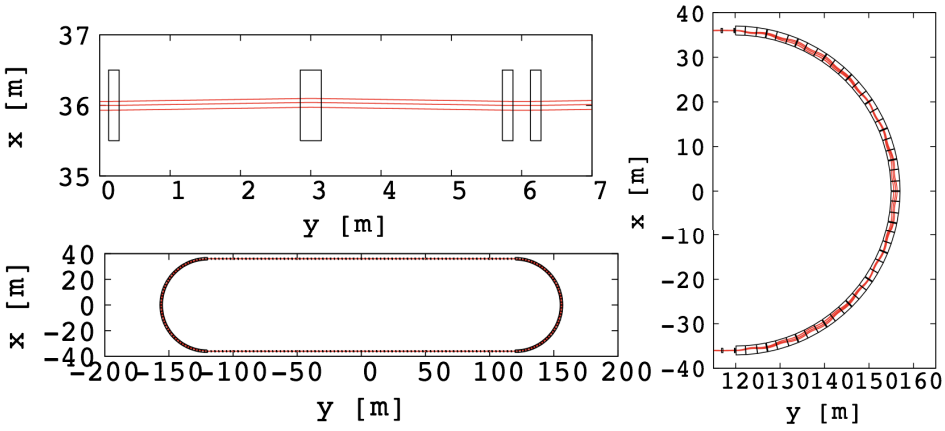

Figure 21. Top view of the racetrack FFAG lattice (bottom left scheme). The top left shows a zoom of the straight section and on the right we show a zoom of the arc section. p_0, p_{min}, and p_{max} muon closed orbits are shown in red. Effective field boundaries with collimators are shown in black.

distribution and the red ones are after 60 turns. No beam loss is observed in 60 turns.

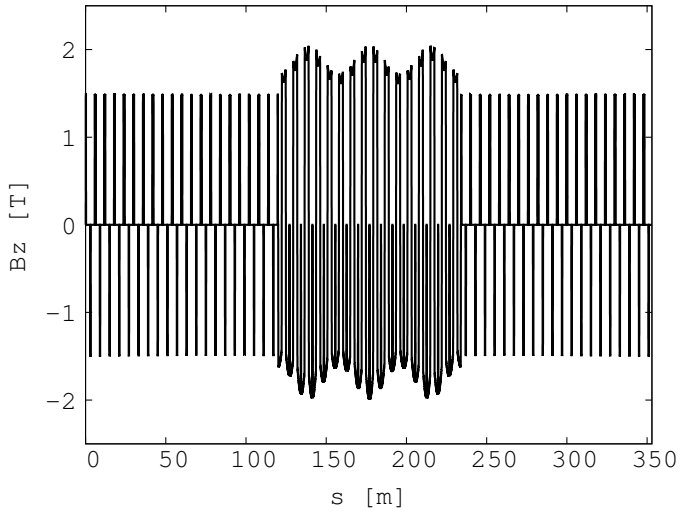

Figure 22. Vertical magnetic field for p_{max} muon closed orbit in the racetrack FFAG ring.

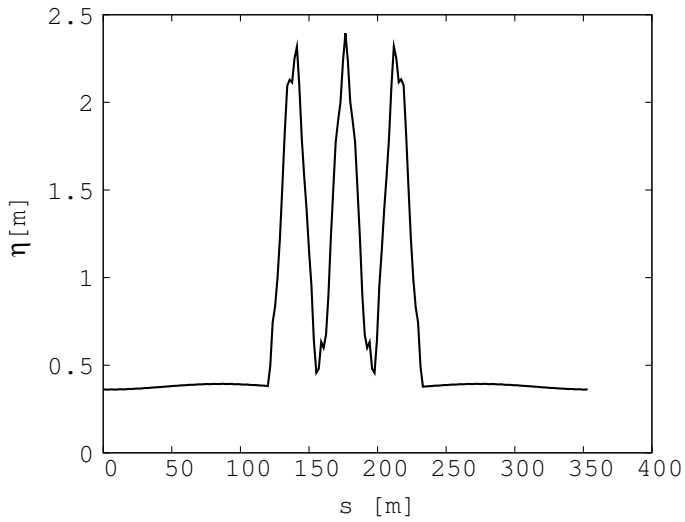

Figure 23. Dispersion function for p_0 in half of the ring. The plot is centered on the arc part.

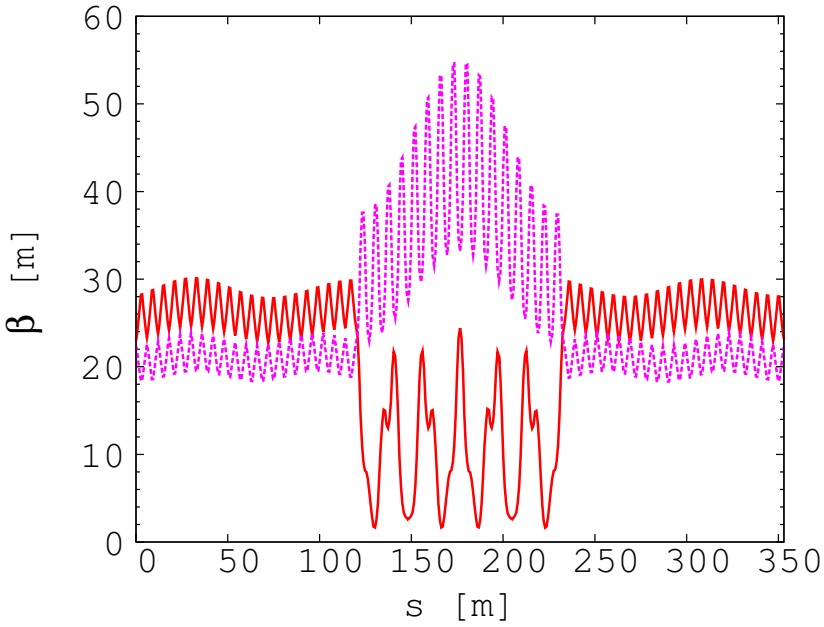

Figure 24. Horizontal (plain red) and vertical (dotted purple) periodic β functions of half of the ring for p_0. The plot is centered on the arc part.

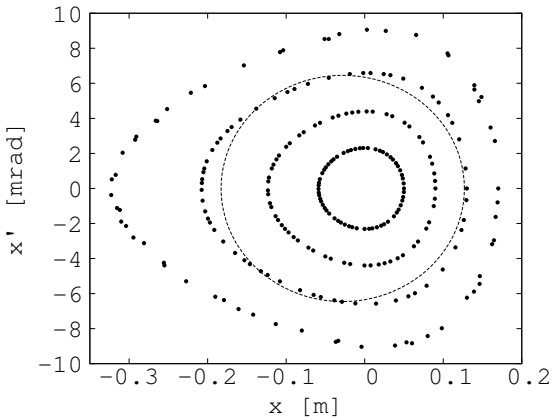

Figure 25. Stable motions in the horizontal Poincare map for different initial amplitudes (5 cm, 9 cm, 13 cm and 17 cm) over 30 turns for p_0. The ellipse shows a 1 mm-radian unnormalized emittance.

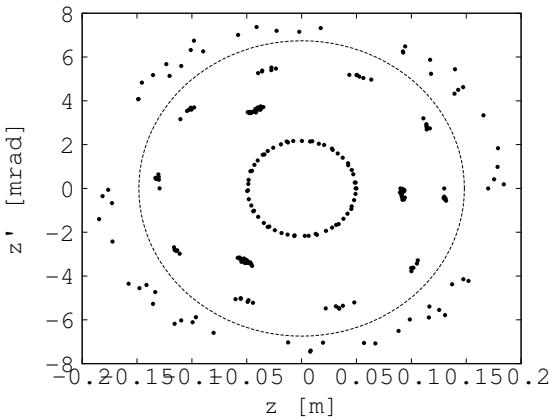

Figure 26. Stable motions in the vertical Poincare map for different initial amplitudes (5 cm, 9 cm, 13 cm and 17 cm) over 30 turns for p_0. The ellipse shows a 1 mm-radian unnormalized emittance.

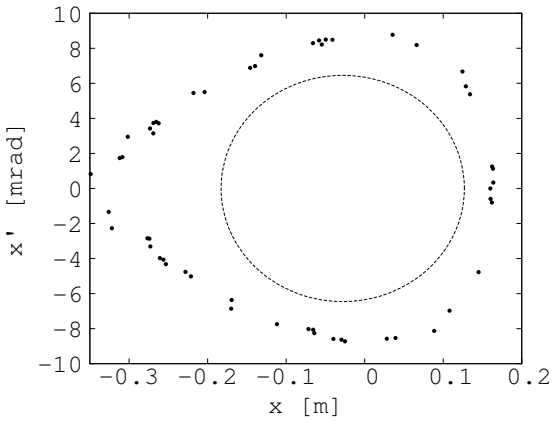

Figure 27. Horizontal Poincare map for maximum initial amplitude (16 cm) with stable motion over 30 turns for p_{min}. The ellipse shows a 1 mm-radian unnormalized emittance.

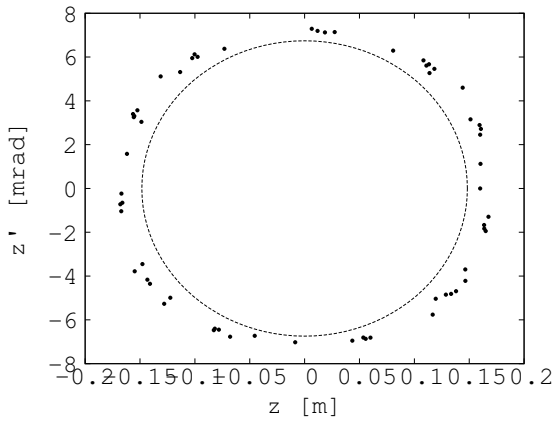

Figure 28. Vertical Poincare map for maximum initial amplitude (16 cm) with stable motion over 30 turns for p_{min}. The ellipse shows a 1 mm-radian unnormalized emittance.

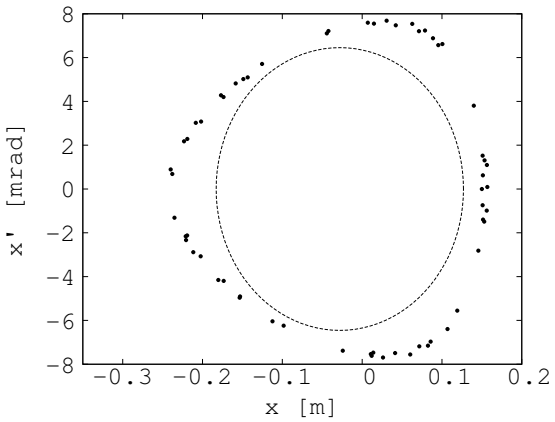

Figure 29. Horizontal Poincare map for maximum initial amplitude (15 cm) with a stable motion over 30 turns for p_{max}. The ellipse shows a 1 mm-radian unnormalized emittance.

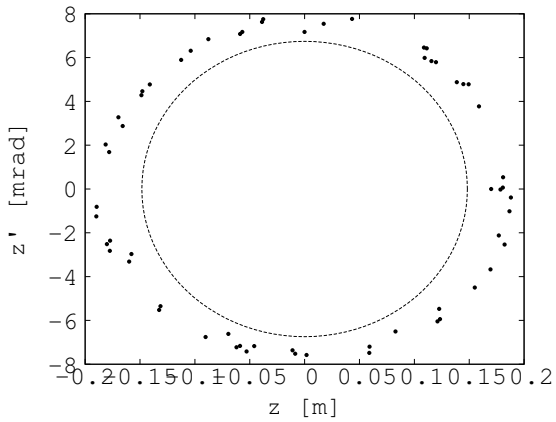

Figure 30. Vertical Poincare map for maximum initial amplitude (17 cm) with a stable motion over 30 turns for p_{max}. The ellipse shows a 1 mm-radian unnormalized emittance.

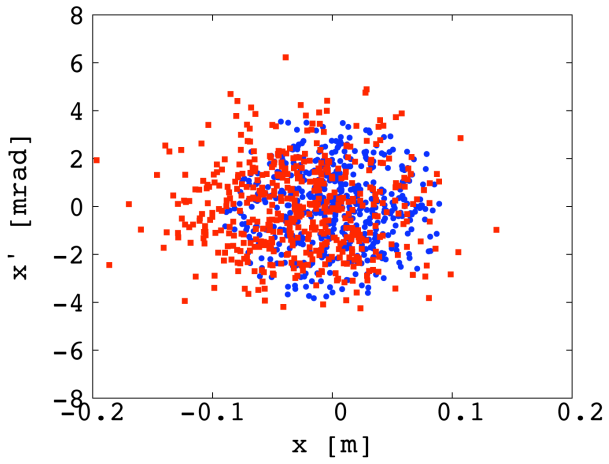

Figure 31. Beam tracking results in the horizontal phase space for a beam with $\Delta p/p_0 = \pm 16\%$. The blue shows the initial particle distribution and the red the final distribution after 60 turns.

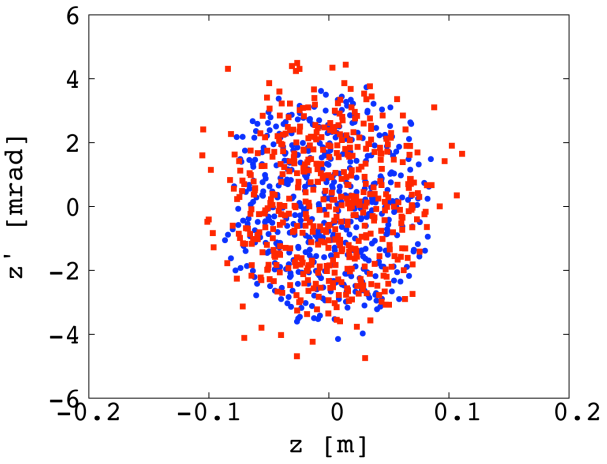

Figure 32. Beam tracking results in the vertical phase space for a beam with $\Delta p/p_0 = \pm 16\%$. The blue shows the initial particle distribution and the red the final distribution after 60 turns.

IV. FAR DETECTOR - SUPERBIND

The Super B Iron Neutrino Detector (SuperBIND) is an iron and scintillator sampling calorimeter which is similar in concept to the MINOS detectors [76]. We have chosen a cross section of approximately 5 m in order to maximize the ratio of the fiducial mass to total mass. The magnetic field will be toroidal as in MINOS and SuperBIND will also use extruded scintillator for the readout planes. Details on the iron plates, magnetization, scintillator, photodetector and electronics are given below. Fig. 33 gives an overall schematic of the detector. We note that within the Advanced European Infrastructures for Detectors

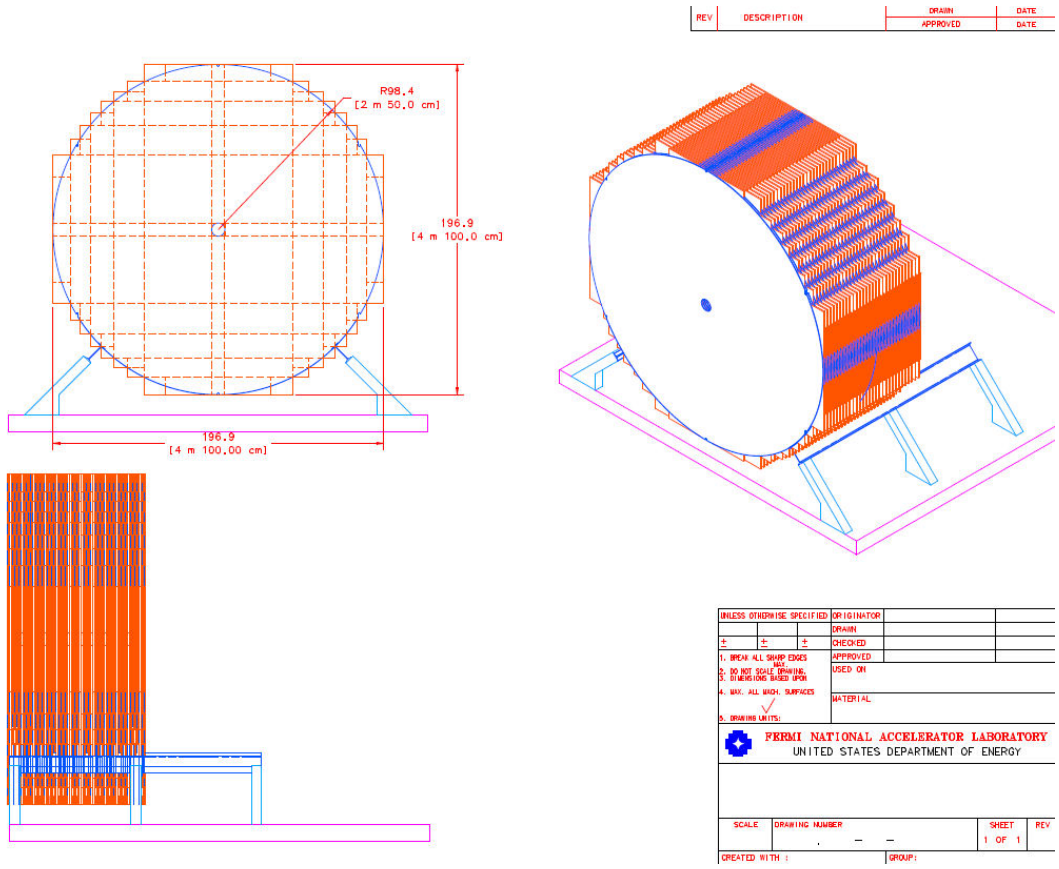

Figure 33. Far Detector concept

at Accelerators (AIDA) project, whose time line runs from 2011 to 2015, detectors similar to those planned for νSTORM will be built and characterized at CERN. The motivation is to test the capabilities for charge identification of $\leq$ 5GeV/c electrons in a Totally Active Scintillator Detector and $\leq$5 GeV/c muons in a Magnetized Iron Neutrino Detector (MIND). These detector prototypes will provide further experience in the use of STL technology, and SiPMs and associated electronics, to complement the already large body of knowledge gained through past and current operation of this type of detector.

A. Iron Plates

For the Iron plates in SuperBIND, we are pursuing the following design strategy. The plates are cylinders with an overall diameter of 5 m and and depth of 1.0 cm. They are fabricated from two semicircles that are skip welded together. Instead of hanging the plates on ears (as was done in MINOS), we plan to stack in a cradle using a strong-back when starting the stacking. We envision that no R&D on the iron plates will be needed. Final specification of the plate structure would be determined once a plate fabricator is chosen.

B. Magnetization

As was mentioned above, MIND will have a toroidal magnetic field like that of MINOS. For excitation, however, we plan to use the concept of the Superconducting Transmission Line (STL) developed for the Design Study for a Staged Very Large Hadron Collider [77]. Minimization of the muon charge mis-identification rate requires the highest field possible in the iron plates. SuperBIND requires a much large excitation current per turn than that of the MINOS near detector (40 kA-turns). We have simulated 3 turns of the STL (20 cm hole). The STL is described in Appendix A and shown in Fig. A 4. Utilizing the SuperBIND plate geometry shown in Fig. 33, a 2-d finite element magnetic field analysis for the plate was performed. Fig. 34 shows the results of those calculations. For this analysis, a 20 cm diameter hole for the STL was assumed, the CMS steel [78] BH curve was used and an excitation current of 250 kA-turn was assumed. This current represents approximately 80% of the critical current achieved at 6.5K in the STL test stand assembled for the VLHC proof-of-principle tests.

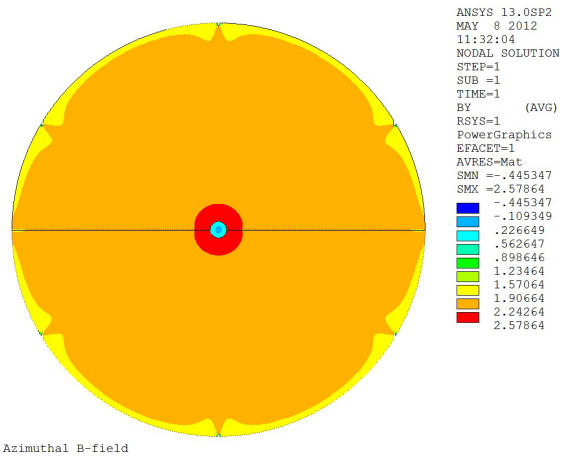

Figure 34. Toroidal Field Map

C. Detector planes

1. Scintillator

Particle detection using extruded scintillator and optical fibres is a mature technology. MINOS has shown that co-extruded solid scintillator with embedded wavelength shifting (WLS) fibres and PMT readout produces adequate light for MIP tracking and that it can be manufactured with excellent quality control and uniformity in an industrial setting. Many experiments use this same technology for the active elements of their detectors, such as the K2K Scibar [79], the T2K INGRID, P0D, and ECAL [80] and the Double-Chooz cosmic-ray veto detectors [81].

Our initial concept for the readout planes for SuperBIND is to have both an x and a y view between each plate. The simulations done to date have assumed a scintillator extrusion profile that is 1.0×1.0 cm^2. This gives both the required point resolution and light yield.

2. Scintillator extrusions

The existing SuperBIND simulations have assumed that the readout planes will use an extrusion that is 1.0×1.0 cm^2. A 1 mm hole down the centre of the extrusion is provided for insertion of the wavelength shifting fibre. This is a relatively simple part to manufacture and has already been fabricated in a similar form for a number of small-scale applications. The scintillator strips will consist of an extruded polystyrene core doped with blue-emitting fluorescent compounds, a co-extruded TiO_2 outer layer for reflectivity, and a hole in the middle for a WLS fibre. Dow Styron 665 W polystyrene pellets are doped with PPO (1% by weight) and POPOP (0.03% by weight). The strips have a white, co-extruded, 0.25 mm thick TiO_2 reflective coating. This layer is introduced in a single step as part of a co-extrusion process. The composition of this coating is 15% TiO_2 in polystyrene. In addition to its reflectivity properties, the layer facilitates the assembly of the scintillator strips into modules. The ruggedness of this coating enables the direct gluing of the strips to each other and to the module skins which results in labour and time savings. This process has now been used in a number of experiments.

D. Photo-detector

Given the rapid development in recent years of solid-state photodetectors based on Geiger mode operation of silicon avalanche photodiodes, we have chosen this technology for SuperBIND. Although various names are used for this technology, we will use silicon photomultiplier or SiPM.

1. SiPM Overview

SiPM is the often-used name for a type of photo detector formed by combining many small avalanche photodiodes operated in the Geiger mode to form a single detector [82, 83]. Detailed information and basic principles of operation of these "multi-pixel" photodiodes can be found in a recent review paper and the references therein [84]. The first generation of these detectors use a polysilicon resistor connected to each avalanche photodiode forming a pixel. Pixels usually vary in size from 10 $\times$10 μm^2 to 100 $\times$ 100 μm^2 (see Figure 35, left). All the diodes are connected to a common electrical point on one side, typically through the substrate, and all the resistors are connected to a common grid with metal traces on the other side to form a two node device. A typical SiPM will have from 100 to 10,000 of these pixels in a single device, with the total area from 1 to 10 mm^2. Because all the diodes and the individual quenching resistors are connected in parallel, the SiPM device as a whole appears as a single diode. In operation, the device appears to act somewhat like a conventional APD, but in detail it is radically different. Because the diodes are operated in the Geiger mode, and because every pixel of the SiPM device is nearly identical, the sum of the fired pixels gives the illusion of an analog signal that is proportional to the incident light, but it is an essentially digital device. The photo counting capabilities of the SiPM are unmatched, as can be seen in Fig. 35 (right) from [85]. SiPMs have a number of advan-

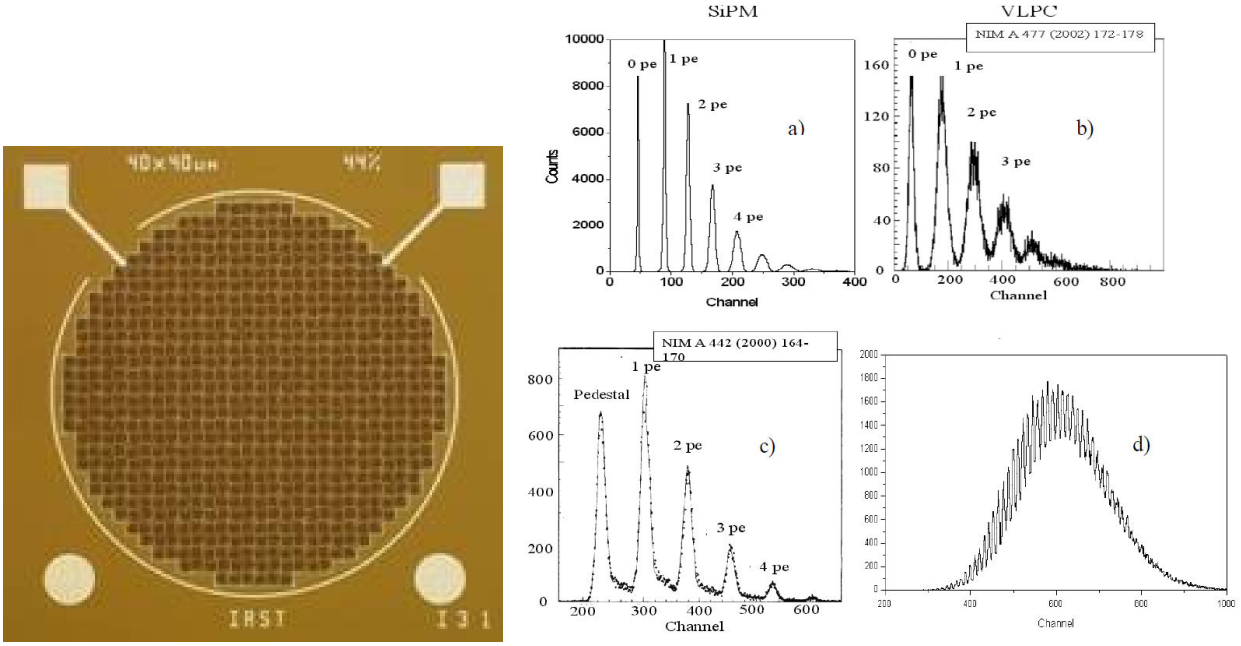

Figure 35. Photograph of SiPM (left) and SiPM photon counting capability (a) compared to VLPC (b) and HPD (c) . The SiPM pulse height spectrum (d) for an intense light burst with a mean photoelectron number of 46 is also shown.

tages over conventional photo multiplier tubes, including high photon detection efficiency, complete immunity to magnetic fields, excellent timing characteristics, compact size and physical robustness. They are immune to nuclear counter effect and do not age. They are

particularly well suited to applications where optical fibers are used, as the natural size of the SiPM is comparable to that of fibers. But the most important single feature of the SiPM is that it can be manufactured in standard microelectronics facilities using well established processing. This means that huge numbers of devices can be produced without any manual labor, making the SiPMs very economical as the number of devices grows. Furthermore, it is possible to integrate the electronics into the SiPM itself, which reduces cost and improves performance. Initial steps have been taken in this direction, though most current SiPMs do not have integrated electronics. But it is widely recognized that this is the approach that makes sense in the long run for many applications. It improves performance and reduces cost, and can be tailored to a specific application. As the use of SiPMs spreads, so will the use of custom SiPM with integrated electronics, just as ASICs have superseded standard logic in micro electronics.

The photon detection efficiency (PDE) of a SiPM is the product of 3 factors:

$$\text{PDE} = QE \cdot \varepsilon_{Geiger} \cdot \varepsilon_{pixel}, \tag{1}$$

where QE is the wavelength-dependent quantum efficiency, ε_{Geiger} is the probability to initiate the Geiger discharge by a photoelectron, and ε_{pixel} is the fraction of the total photodiode area occupied by sensitive pixels. The bias voltage affects one parameter in the expression (1), ε_{Geiger}. The geometrical factor ε_{pixel} is completely determined by the photodiode topology, and is in the range 50-70%. The PDE of a device manufactured by Hamamatsu (Hamamatsu uses the name multi-pixel photon counter, MPPC) as function of wavelength of detected light is shown in Figure 36.

2. Readout Electronics

Currently, a number of companies are working on integrating electronics and SiPM detectors on the same device, on the same wafer. The first such device was announced by Philips in 2009 and a complete system for evaluation of this technology is commercially available. The system features a fully digital SiPM with active quenching and it is reasonable to expect that this technology will continue to advance and new devices with lower costs and better performance will appear. However, one important disadvantage of integrating electronics with the photodetector is that the SiPM becomes an ASIC, an Application Specific Integrated Circuit, and it is much more likely that additional R&D will be required to develop the system. The question then becomes what level of investment in research and development is justified in order to optimize the detector for the particular application described here. Clearly, it is much too early to answer this question, but generally we can outline three possible approaches, given the current state of SiPM development.

The first approach is to pursue commercially available “analog” SiPMs coupled to commercially available, “off the shelf” electronics. This approach is often referred to as “COTS”.

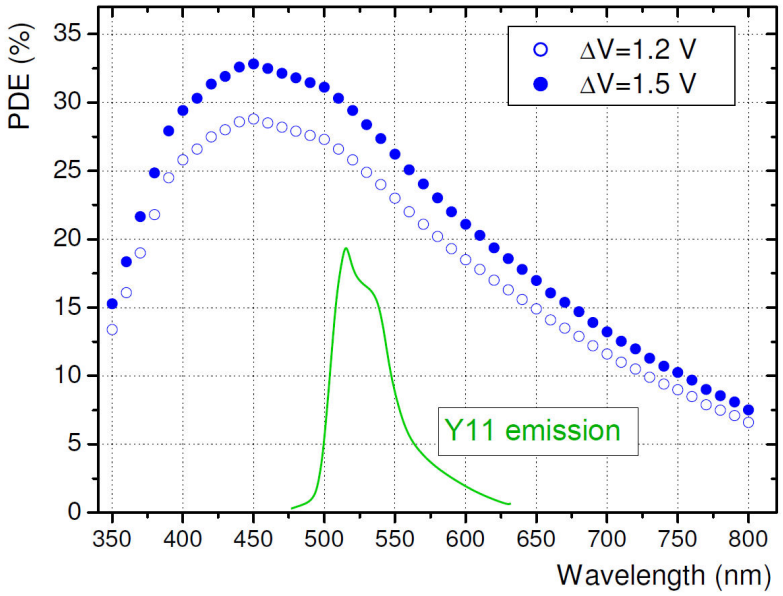

Figure 36. Photon detection efficiency of a Hamamatsu MPPC as a function of wavelength of the detected light at ΔV of 1.2 and 1.5 V at 25°C. The Y11(150 ppm) Kuraray fiber emission spectrum for a fiber length of 150 cm (from Kuraray specification) is also shown.

This is the approach taken so far by existing experiments and those planned for the near future. This includes T2K, mu2e and CALICE. This has the advantage of low technical risk and has a well understood cost. A typical implementation of the electronics might be based on commercial AFE (analog front end) chips and FPGAs, with Ethernet readout. An example of a preliminary prototype for mu2e is shown in Fig. 37. Another approach would

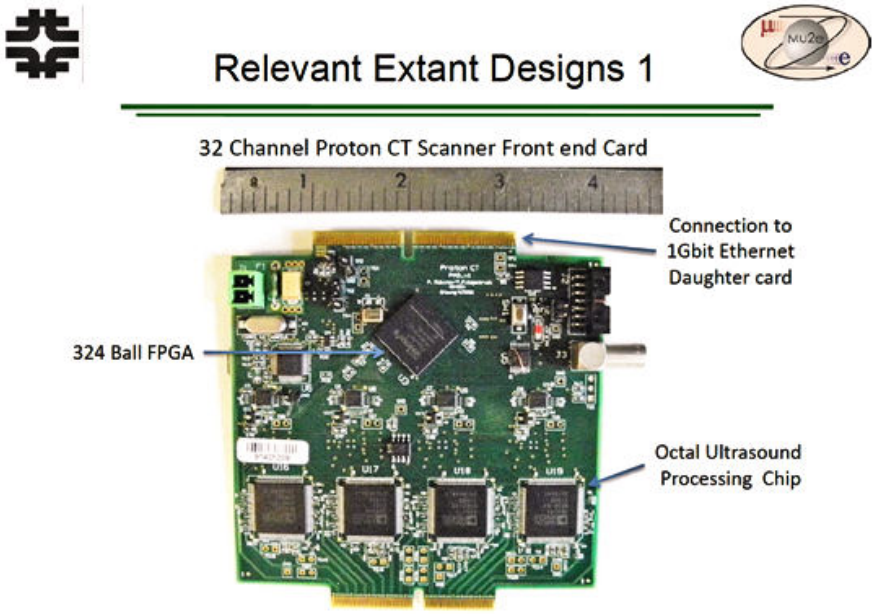

Figure 37. 32 channel SiPM readout card based on commercially available electronics.

be to adopt existing SiPMs to an existing ASIC designed specifically for SiPMs. This is not the same as developing a custom ASIC, as these devices already exist for some other experiments. There are many similarities between different experiments in high energy physics and the popularity and interest in SiPMs is driving development for various applications. Some examples of ASICs that have been used (or are being developed for use) with SiPMs are the TriP-t (developed at Fermilab for Dzero, now used by T2K for SiPM readout), TARGET (developed for Cherenkov Telescope Array) [86] as well as the EASIROC, the SPIROC and their derivative chips that were developed by the Omega group at IN2P3 in Orsay. The third approach is to develop a custom solution, using either analog or digital SiPMs. This approach could potentially significantly reduce the per channel cost of both the photodetector and electronics, but involves higher technical risk and requires larger initial investment. This is clearly the best approach for a sufficiently large detector system, but more resources would need to be devoted to make a specific proposal for a custom SiPM development. One possible approach would be to slightly modify an existing SiPM to allow many connections between the SiPM and the readout ASIC. This is essentially a hybrid solution with a "near digital" SiPM, where a few SiPM pixels are wire bonded to an electronics channel. This would provide most of the benefits of digital SiPMs, but with a much shorter and simpler development effort. A conceptual design is show in Fig. 38

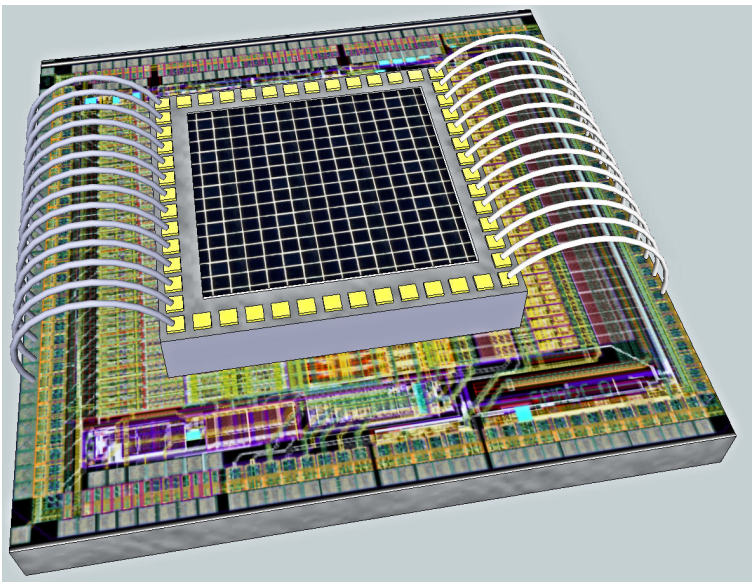

Figure 38. A possible configuration for a hybrid approach is shown. The top chip is a SiPM, wire bonded to a readout chip on the bottom.

V. NEAR DETECTORS

The near detector hall at νSTORM presents opportunities for both oscillation physics and neutrino cross section measurements. We have assumed that the hall will be located at $\sim$ 50m from the end of the straight. The neutrino flux at this position has been calculated and the representative number of events (per 100T fiducial mass) for our 10^{21} POT exposure is given in Fig. 39, left for ν_e and right for $\bar{\nu}_\mu$.

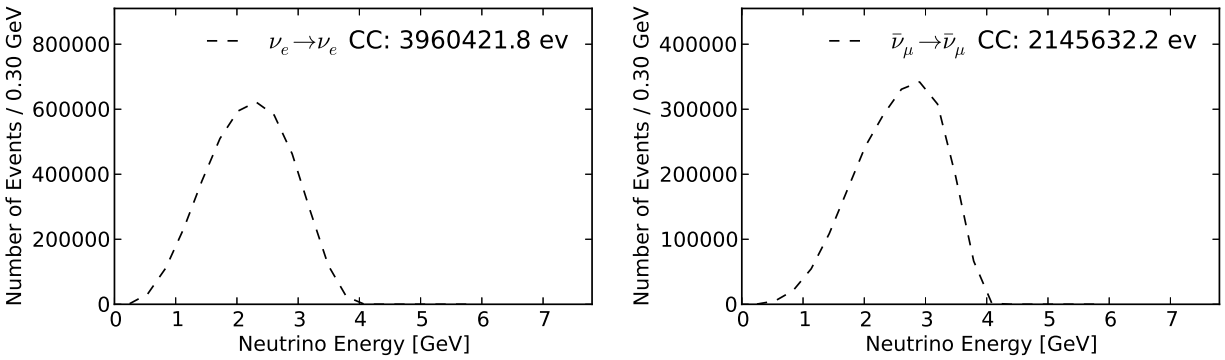

Figure 39. ν_e spectrum at near detector (Left), $\bar{\nu}_\mu$ (Right).

Channel	N_{evts}
$\bar{\nu}_\mu$ NC	844,793
ν_e NC	1,387,698
$\bar{\nu}_\mu$ CC	2,145,632
ν_e CC	3,960,421

Table V. Event rates at near detector (for 100T) with μ^+ stored

Channel	N_{evts}
$\bar{\nu}_e$ NC	709,576
ν_μ NC	1,584,003
$\bar{\nu}_e$ CC	1,784,099
ν_μ CC	4,626,480

Table VI. Event rates at near detector (for 100T) with μ^- stored

A. For short-baseline oscillation physics

A near detector is needed for the oscillation disappearance searches and our concept (detailed stuides have not yet been done for these channels) is to build a near detector that is identical to SuperBIND, but with approximately 100-200T of fiducial mass. A muon "catcher" will most likely be needed in order to maximize the usefulness of the "as-built" detector mass. Before a final specification for this near detector can be made, full simulation and analysis for the disappearance channels will have to be done.

B. HIRESMNU: A High Resolution Detector for ν interaction studies

Precision measurements of neutrino-interactions at the near-detector (ND) are necessary to ensure the highest possible sensitivity for neutrino oscillation studies (both for νSTORM and for any future long-baseline neutrino oscillation experiment). Regardless of the process under study — $\boldsymbol{\nu_\mu \rightarrow \nu_e}$ ($\boldsymbol{\bar{\nu}_\mu \rightarrow \bar{\nu}_e}$) appearance or $\boldsymbol{\nu_\mu}$ ($\boldsymbol{\bar{\nu}_\mu}$) disappearance — the systematic error should be less than the corresponding statistical error. A near detector concept which will well suit ths purpose is the high resolution detector, HIRESMNU, proposed for the LBNE project [87]. It can fulfill four principal goals:

1. Measurement of the absolute and the relative abundance of the **four** species of neutrinos, $\boldsymbol{\nu_\mu}$, $\boldsymbol{\bar{\nu}_\mu}$, $\boldsymbol{\nu_e}$, and $\boldsymbol{\bar{\nu}_e}$, as a function of energy ($\boldsymbol{E_\nu}$). Accurate determination of the angle and the momentum of the electron in neutrino-electron neutral current interaction will provide the absolute flux.

2. Determination of the absolute $\boldsymbol{E_\nu}$-scale, a factor which determines value of the oscillation-parameter Δm^2.

3. Determination of $\boldsymbol{\pi^0}$'s and $\boldsymbol{\pi^+/\pi^-}$'s produced in the NC and CC interactions. The pions are the predominant source of background for any oscillation study.

4. Measurement of ν-Nucleus cross-section where the nuclear target will be that of the far-detector. The cross-section measurements of exclusive and inclusive CC and NC processes will furnish a rich panoply of physics relevant for most neutrino research. Knowing the cross sections at the $\boldsymbol{E_\nu}$ typical of the νSTORM beam is essential for predicting both the signal and the background.

Figure 40 shows a schematic of this the HIRESMNU design. The architecture [87] derives from the experience of NOMAD [88]. It embeds a $4 \times 4 \times 7$ m^3 STT and a surrounding 4π electromagnetic calorimeter (ECAL) in a dipole magnet with $B \simeq 0.4$ T. Downstream of the magnet and additionally within the magnet yoke are detectors for muon identification. The STT will have a low average density similar to liquid hydrogen, about 0.1 gm/cm^3, which is essential for the momentum determination and ID of electrons, protons, and pions. The foil layers interleaved with the straw tubes contribute most of the 7 ton fiducial mass. The foil layers serve both as the mass on which the neutrinos will interact and as generators of transition radiation (TR), which aids in electron identification. Its depth in radiation lengths is sufficient for 50% of the photons from $\boldsymbol{\pi^0}$ decay to be observed as e^+e^- pairs, which delivers superior resolution compared with conversions in the ECAL. Layers of nuclear-targets will be deployed at the upstream end of the STT for the determination of cross sections on these materials. The HIRESMNU delivers the most sensitive systematic constraints as studied within the LBNE context. The systematic studies include ν-electron scattering, quasi-elastic interactions, $\boldsymbol{\nu_e/\bar{\nu}_e}$-CC, neutral-current identification, $\boldsymbol{\pi^0}$ detection, etc. The quoted dimensions, mass, and segmentation of HIRESMNU will be further optimized for νSTORM as the proposal evolves.

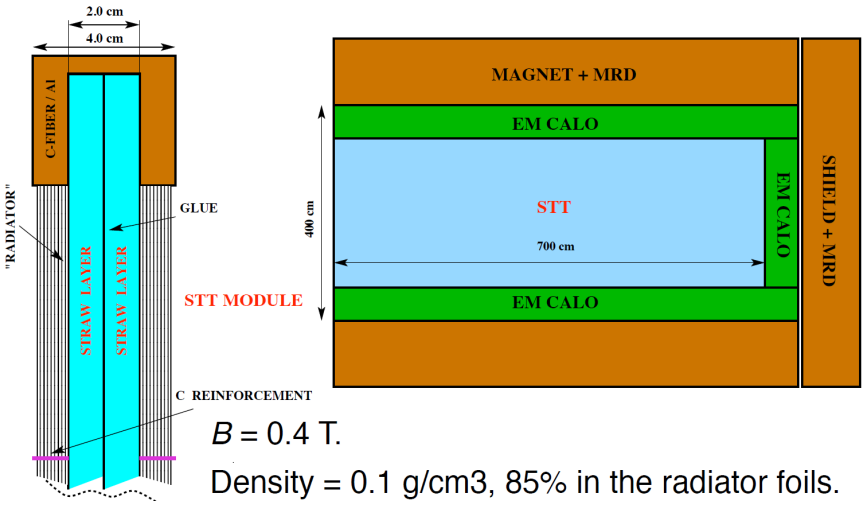

Figure 40. Schematic of the ND showing the straw tube tracker (STT), the electromagnetic calorimeter (ECAL) and the magnet with the muon range detector (MRD). The STT is based upon ATLAS [89] and COMPASS [90] trackers. Also shown is one module of the proposed straw tube tracker (STT). Interleaved with the straw tube layers are plastic foil radiators, which provide 85% of the mass of the STT. At the upstream end of the STT are layers of nuclear-target for the measurement of cross sections and the $\boldsymbol{\pi^0}$'s on these materials.

VI. PERFORMANCE

A. Event rates

The number of muon decays (N_μ) for νSTORM can be defined in terms of the following:

$$N_\mu = (\text{POT}) \times (\pi \text{ per POT}) \times \epsilon_{\text{col}} \times \epsilon_{\text{trans}} \times \epsilon_{\text{inj}} \times (\mu \text{ per } \pi) \times A_{\text{dyn}} \times \Omega \qquad (2)$$

where (POT) is the number of protons on target, ϵ_{col} is the collection efficiency, ϵ_{trans} is the transport efficiency, ϵ_{inj} is the injection efficiency, (μ per π) is the chance that an injected pion results in a muon within the ring acceptance, A_{dyn} is the probability that a muon within the decay ring aperture is within the dynamic aperture, and Ω is the fraction of the ring circumference that directs muons at the far detector. νSTORM assumes 10^{21} POT for a 4-5 year run using 60 GeV protons. From section III A, we obtain (with horn collection) $\simeq 0.1\pi$/pot$\times$collection efficiency. We have assumed that the transport efficiency, and the injection efficiency are 0.8 and 0.9, respectively and that the probability that a π decay results in a μ within the acceptance $\times\gamma c\tau$ is 0.08. Ω is 0.34. This results in approximately 2 $\times 10^{18}$ useful μ decays. With a 1kT fiducial mass far detector located at approximately 2 km from the end of the decay ring straight, we have the following raw event rates: In addition to the μ decay beam, we also have a high-intensity π decay neutrino beam, $\overset{(-)}{\nu}_\mu$, from the straight section (at injection into the ring) which can easily be time separated from the μ decay beam. This $\overset{(-)}{\nu}_\mu$ is roughly the same intensity as the integrated $\overset{(-)}{\nu}_\mu$ beam from the stored μ decays.

Channel	$N_{\text{osc.}}$	N_{null}	Diff.	$(N_{\text{osc.}} - N_{\text{null}})/\sqrt{N_{\text{null}}}$
$\nu_e \to \nu_\mu$ CC	332	0	∞	∞
$\bar{\nu}_\mu \to \bar{\nu}_\mu$ NC	47679	50073	-4.8%	-10.7
$\nu_e \to \nu_e$ NC	73941	78805	-6.2%	-17.3
$\bar{\nu}_\mu \to \bar{\nu}_\mu$ CC	122322	128433	-4.8%	-17.1
$\nu_e \to \nu_e$ CC	216657	230766	-6.1%	-29.4
Channel	$N_{\text{osc.}}$	N_{null}	Diff.	$(N_{\text{osc.}} - N_{\text{null}})/\sqrt{N_{\text{null}}}$
$\bar{\nu}_e \to \bar{\nu}_\mu$ CC	117	0	∞	∞
$\bar{\nu}_e \to \bar{\nu}_e$ NC	30511	32481	-6.1%	-10.9
$\nu_\mu \to \nu_\mu$ NC	66037	69420	-4.9%	-12.8
$\bar{\nu}_e \to \bar{\nu}_e$ CC	77600	82589	-6.0%	-17.4
$\nu_\mu \to \nu_\mu$ CC	197284	207274	-4.8%	-21.9

Table VII. Truth event rates for 10^{21} POT for best-fit values for the LSND anomaly figure-of-merit.

B. Monte Carlo and analysis

1. Neutrino event generation and detector simulation

The Monte Carlo and analysis for the SuperBIND detector is closely based on the simulations and analysis of the MIND detector for the Interim Design Report of the International Design Study for a Neutrino factory (IDS-NF) [4]. Generation for all types of interactions was performed using the GENIE framework [91]. The simulation of the generated events was carried out using the GEANT4 toolkit [92] (version 4.9.4), with full hadron shower development and digitization of the events. The simulated detector was the SuperBIND detector described in section IV, cylindrical in shape with a 5 m diameter and 20 m in length. Each of the individual modules were composed of alternating 1 cm thick iron plates and 2 cm planes of polystyrene extruded plastic scintillator in two views (one along the x axis and the other along the y axis). Simulations with 2 cm iron plates were also carried out in order to optimize the geometric configuration. A toroidal magnetic field is simulated inside the iron. The amplitude of the field is parameterized as a function of radius r according to the following:

$$B(r) = B_0 + \frac{B_1}{r} + B_2 e^{-Hr}, \tag{3}$$

with $B_0 = 1.53$ T, $B_1 = 0.032$ T·m, $B_2 = 0.64$ T and $H = 0.28$ m^{-1}. The field and its parametrisation along the 45° azimuth direction are shown in Fig. 41.

Events generated for iron and scintillator nuclei are selected according to their relative weights in the detector and the resultant particles are tracked from a vertex randomly positioned in three dimensions within a randomly selected piece of the appropriate material. Physics processes are modelled using the QGSP_BERT physics lists provided by GEANT4 [93]. Secondary particles are required to travel at least 30 mm from their production point

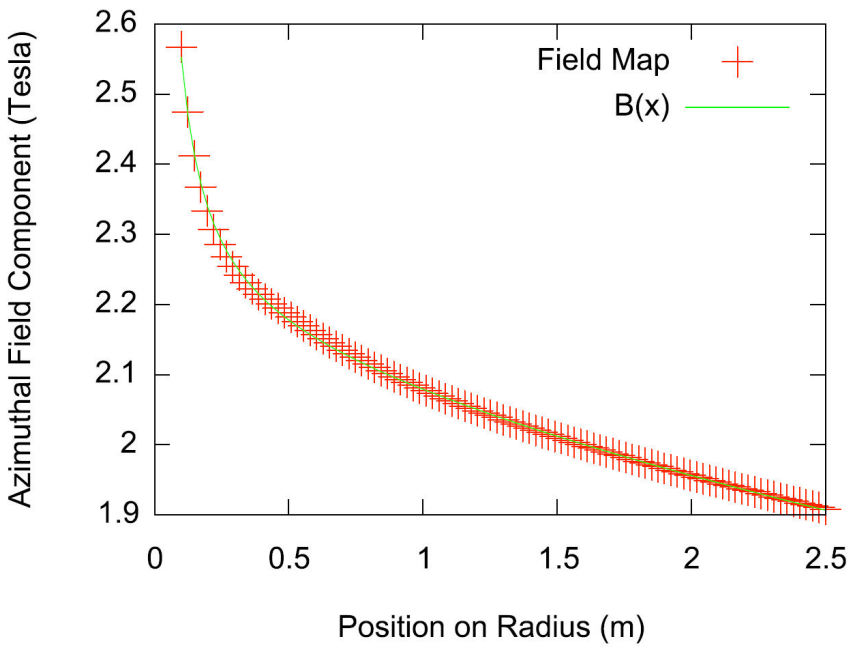

Figure 41. Radial parametrisation of the toroidal magnetic field in SuperBIND along the 45° azimuth direction.

or to cross a material boundary between the detector sub-volumes to have their trajectory fully tracked. Generally, particles are only tracked down to a kinetic energy of 100 MeV. However, gammas and muons are excluded from this cut.

A simplified digitisation model was considered for this simulation. Two-dimensional boxes with 1 cm edge length – termed voxels – represent view-matched x and y scintillator readout positions. The response of the scintillator bars is derived from the raw energy deposited in each voxel, read out using wavelength shifting (WLS) fibres with an attenuation length $\lambda = 5$ m, as reported by the Minerνa collaboration [94]. Assuming that approximately half of the energy will come from each view, the deposit is halved and the remaining energy at each edge in x and y is calculated. This energy is then smeared according to a Gaussian width $\sigma/E = 6\%$ to represent the response of the electronics and then recombined into E_x, E_y and total energy $= E_x + E_y$ energy deposited per voxel. An output wavelength of 525 nm, a photo-detector quantum efficiency of $\sim$30% and a threshold of 4.7 photo electrons (pe) per view (as in MINOS [76]) were assumed. Any voxel view that is not above the threshold is cut.

The simulation was run assuming that the storage ring contains 3.8 GeV/c μ^+, so that the wrong sign muon signal consists of μ^- tracks from ν_μ charged current (CC) interactions. The backgrounds consist of mis-identified μ^+ tracks, and tracks constructed from showers generated by $\bar{\nu}_\mu$ neutral current (NC) and ν_e CC events. The neutrino fluxes were provided as oscillated ν_μ and un-oscillated $\bar{\nu}_\mu$ and ν_e spectra. The exclusive event spectra generated by GENIE are shown in Fig. 42. The appropriate flux spectrum was input into the GENIE simulation to provide the samples of neutrino interaction events passed to the GEANT4

simulation.

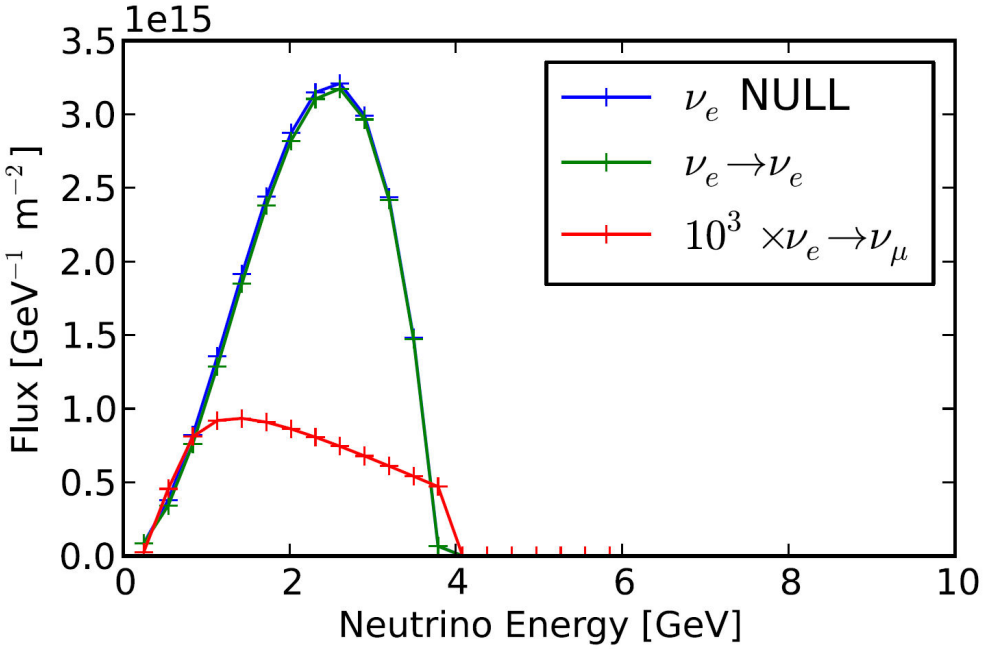

Figure 42. Neutrino fluxes used to carry out the simulations of the SuperBIND detector.

2. Event reconstruction

The reconstruction package was described in detail in [95] and in the Interim Design Report of the IDS-NF [4]. The first stage of the reconstruction includes a clustering algorithm [96]. The clusters formed from the hit voxels of an event are then passed to the reconstruction algorithm. The separation of candidate muons from hadronic activity is achieved using two methods: a Kalman filter algorithm provided by RecPack [97] and a cellular automaton method (based on [98]), both algorithms are described in detail in [95].

Fitting of the muon candidates proceeds using a Kalman filter to fit a helix to the candidate, using an initial seed estimated from the path length of the muon track, using the Continuous Slowing Down Approximation (CSDA [99]), and then refitting any successes. Neutrino energy is generally reconstructed as the sum of the muon and hadronic energies, with hadronic reconstruction currently performed using a smear on the true quantities as described in reference [95]. The reconstruction of the hadronic energy E_{had} (in GeV) assumes a resolution δE_{had} from the MINOS CalDet testbeam [76, 100] (although we believe that SuperBIND will do better):

$$\frac{\delta E_{had}}{E_{had}} = \frac{0.55}{\sqrt{E_{had}}} \oplus 0.03. \tag{4}$$

The hadronic shower direction vector is also smeared according to the angular resolution found by the Monolith test-beam [101]:

$$\delta\theta_{had} = \frac{10.4^\circ}{\sqrt{E_{had}}} \oplus \frac{10.1^\circ}{E_{had}}. \tag{5}$$

In the case of QE interactions, where there is no hadronic jet, the neutrino energy reconstruction was carried out using the formula:

$$E_\nu = \frac{m_N E_\mu + \frac{1}{2}\left(m_{N'}^2 - m_\mu^2 - m_N^2\right)}{m_N - E_\mu + |p_\mu| \cos\vartheta}\,; \tag{6}$$

where ϑ is the angle between the muon momentum vector and the beam direction, m_N is the mass of the initial state nucleon, and $m_{N'}$ is the mass of the outgoing nucleon for the interactions $\nu_\mu + n \to \mu^- + p$ and $\overline{\nu}_\mu + p \to \mu^+ + n$ (see for example [102]).

The iron plate thickness of the detector was studied from the point of view of muon charge identification efficiency. The charge selection efficiency was studied using 1 cm iron plates and 2 cm iron plates. By doubling the thickness of the iron plate, we effectively increase the effective magnetic field between measurments by 50% so the net charge selection efficiency increases, at the expense of a small increase in the threshold. Both of these effects were studied in detail in the following data analysis section.

C. Data Analysis

The basis for the $\nu_e \to \nu_\mu$ analysis closely follows the one for the MIND detector at a Neutrino Factory [4], but was adapted for the lower muon energy of 3.8 GeV. The cuts to reject charged current (CC) and neutral current (NC) backgrounds are organised as follows:

- Successful reconstruction.
- Fiducial volume cut.
- Maximum momentum cut.
- Fitted proportion of hits allocated to the muon track.
- Track quality cuts.
- Neutral current rejection cut.

We commence by imposing the reconstruction criteria from the previous section to guarantee fully reconstructed neutrino events. We then proceed to impose a fiducial cut, requiring that the first cluster in a candidate be at least 1 m from the end of the detector ($z \leq 19000$ mm for a 20 m long detector). The isolated clusters that form a muon track candidate are fitted to determine the muon momentum. A maximum value for the reconstructed muon momentum is imposed at 6.1 GeV (60% above the maximum muon momentum) to remove backgrounds caused by poorly reconstructed momenta. Any remaining clusters are assumed to be part of the hadronic component of the event. Charged current events have a larger proportion

Table VIII. Description of cuts used in the selection of good events from the simulation.

Event Cut	Description
Successful Reconstruction	Failed Kalman reconstruction of event removed
Fiducial	First hit of event is more than 1 m from end of detector
Maximum Momentum	Muon momentum less than $1.6\times E_\nu$
Fitted Proportion	60% of track nodes used in final fit.
Track Quality	$\log(P(\sigma_{q/p}/(q/p)\|CC)/P(\sigma_{q/p}/(q/p)\|NC)) > -0.5$
NC Rejection (1 cm plates)	$\log(P(N_{hit}\|CC)/P(N_{hit}\|NC)) > 6.5$

of hits allocated to the muon candidate. We only accept those events in which more than 60% of its clusters are fitted as a muon candidate, to reduce neutral current and electron neutrino background levels.

The track quality cut is based on the relative error in the inverse momentum of the candidate muon $\frac{\sigma_{q/p}}{q/p}$, where q is the charge of the muon and p its momentum. A Probability Density Function (PDF) $P\left(\sigma_{q/p}/(q/p)\right)$ is created for both CC signal and NC background. The log-likelihood ratio $\mathcal{L}_{q/p}$ between the two distributions is created. The signal events are selected as those with a log-likelihood parameter $\mathcal{L}_{\sigma/p} > -0.5$.

The final cut involves the rejection of neutral current backgrounds, by exploiting the property that ν_μ CC events tend to have greater length than NC events. Hence, the number of hits, N_{hit}, was used to generate Probability Density Functions (PDF) for charged and neutral current events. The log-likelihood ratio rejection parameter:

$$\mathcal{L}_1 = \log\left(\frac{P(N_{hit}|CC)}{P(N_{hit}|NC)}\right) ; \tag{7}$$

is used for NC rejection. For the detector geometry with 1 cm thick plates, the chosen cut $\mathcal{L}_1 > 6.5$ allows the background to be rejected to a level below 10^{-3}. For the case in which we have 2 cm thick plates, the intrinsic NC background is smaller. This analysis is similar but simpler than the MIND analysis for a Neutrino Factory [**?**]. The cuts are summarised in Table VIII.

The effect of the selection criteria on the signal and background simulations is shown in Table IX. Figure 43 shows the fractional efficiency as a function of neutrino energy after these cuts are applied, for the 1 cm iron plate geometry (left) and 2 cm plate geometry (right). Figure 44 shows the fractional backgrounds for the 1 cm plate (left) and 2 cm plates (right). In summary, the cuts described in this section lead to an absolute efficiency of 33% for ν_μ CC selection, while reducing the total background to a level of 5×10^{-4} for the 1 cm plates, while the ν_μ CC selection efficiency is 25% for 2 cm iron plates, with a total background level less than 7×10^{-5}. This analysis would suggest that 2 cm plates are preferred for the neutrino oscillation ν_μ appearance channel. However, this would need to be compared to the ν_e disappearance channel to determine which of the two geometries would be preferred, so further detector optimizations are needed to be able to make a decision on

the optimal geometry.

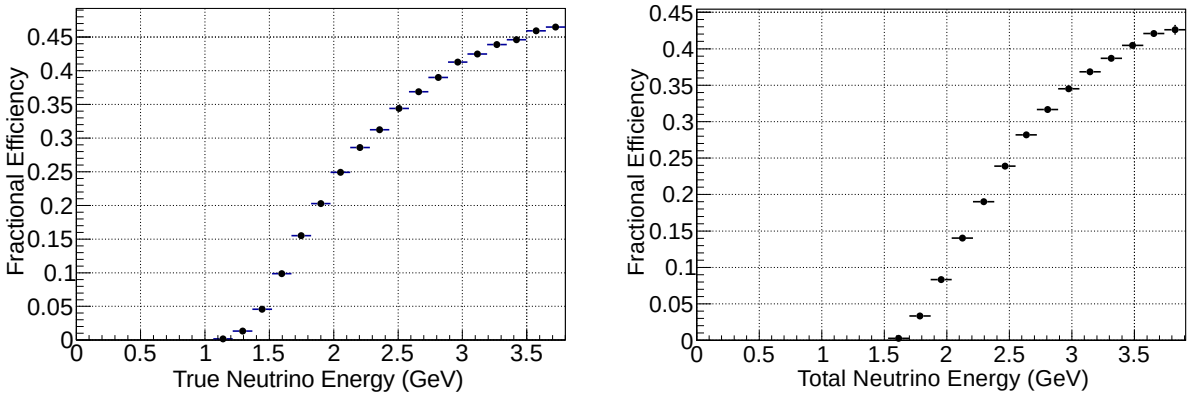

Figure 43. Efficiency of detection of a μ^- signal for a sample of ν_μ Charge Current interactions stopping in a SuperBIND detector with 1 cm iron plates (left) and 2 cm iron plates (right).

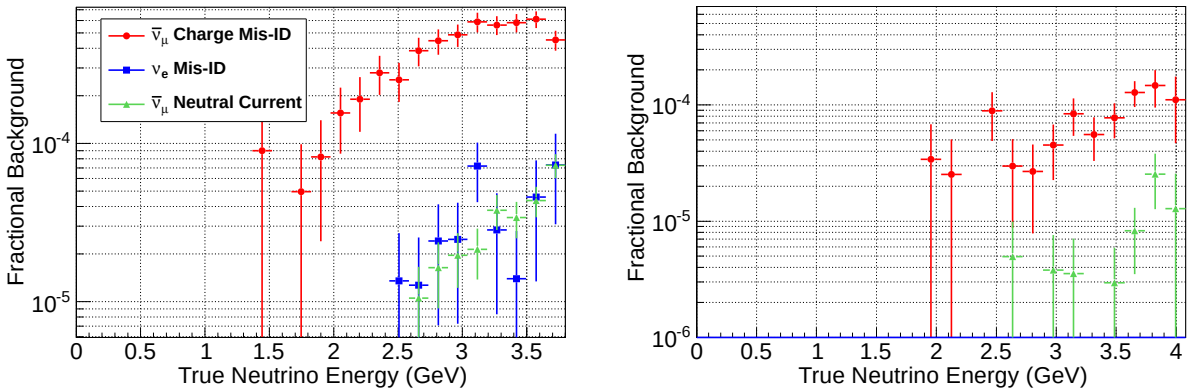

Figure 44. Backgrounds for the detection of a μ^- signal in a SuperBIND detector with 1 cm iron plates (left) and 2 cm iron plates (right) that will be present when μ^+ are contained in the νSTORM storage ring.

D. Sensitivities

From Table VII we see that there are numerous channels in which new physics can be explored. The statistical significance of NC disappearance is 20σ and 16σ for stored μ^+ and μ^-, respectively, if we combine the ν_e and ν_μ NC events together. Appearance physics via the channel $\nu_e \to \nu_\mu$ gives νSTORM broad sensitivity to sterile physics and directly tests the LSND/MiniBooNE anomaly. The oscillation probabilities for both appearance and

Table IX. Fraction of events remaining after cuts are applied to simulations of the indicated species in the nominal SuperBIND detector using 1 cm plates when the appearance of a μ^- in an event is defined as the experimental signal. The final line shows the final event fractions for a detector with 2 cm plates.

	Interaction Type and Species			
Event Cut	ν_μ CC(%)	$\bar{\nu}_\mu$ CC ($\times 10^3$)	ν_e CC ($\times 10^3$)	$\bar{\nu}_\mu$ NC ($\times 10^3$)
Successful Reconstruction	71.9%	38.9	306	99.0
Fiducial	69.4%	31.0	292	94.8
Maximum Momentum	68.1%	24.2	253	80.5
Fitted Proportion	67.3%	22.5	245	75.5
Track Quality	59.6%	7.4	42.8	18.7
NC Rejection (1 cm plates)	33.3%	0.45	0.02	0.03
NC Rejection (2 cm plates)	25.2%	0.065	0.0	0.004

disappearance physics are:

$$\mathrm{P}_{\nu_e \to \nu_\mu} = \quad 4|U_{e4}|^2|U_{\mu 4}|^2 \sin^2\left(\frac{\Delta m^2_{41} L}{4E}\right), \tag{8}$$

$$\mathrm{P}_{\nu_\alpha \to \nu_\alpha} = 1 - [4|U_{\alpha 4}|^2(1 - |U_{\alpha 4}|^2)] \sin^2\left(\frac{\Delta m^2_{41} L}{4E}\right). \tag{9}$$

1. Appearance channels

The appearance signal which the detector is designed for is $\nu_e \to \nu_\mu$; the CPT conjugate of the LSND anomaly $\bar{\nu}_\mu \to \bar{\nu}_e$. For nonzero appearance probability in sterile neutrino models, there must simultaneously be both ν_e and ν_μ disappearance since $|U_{e4}||U_{\mu 4}| \neq 0$, which allows for testing if the LSND anomaly is due to breaking of Lorentz Invariance. Both U_{e4} and $U_{\mu 4}$ must be small resulting in a double suppressed appearance signal unlike the single suppressed disappearance measurements. More sensitivity arises from appearance physics than disappearance physics because backgrounds are more suppressed for wrong-sign muon searches. Assuming oscillations of the type indicated by LSND are present, the following two tables show the event rates between the null hypothesis of no oscillations versus LSND best-fit oscillations. Assuming oscillations of the type indicated by LSND are present, Table VII shows the event rates between the null hypothesis of no oscillations versus LSND best-fit oscillations.

The raw event rates in Table VII indicate the level of background rejection required to extract the $e \to \mu$ oscillations. Detector simulation reveal both the energy smearing matrix and the probability that an event is included as signal. These simulations have been performed for all channels present at this facility (see Section VI C. The χ^2 shown includes only statistical uncertainties. Fig. 45) gives the spectrum for the expected signal and background levels for stored μ^+ given the analysis from above.

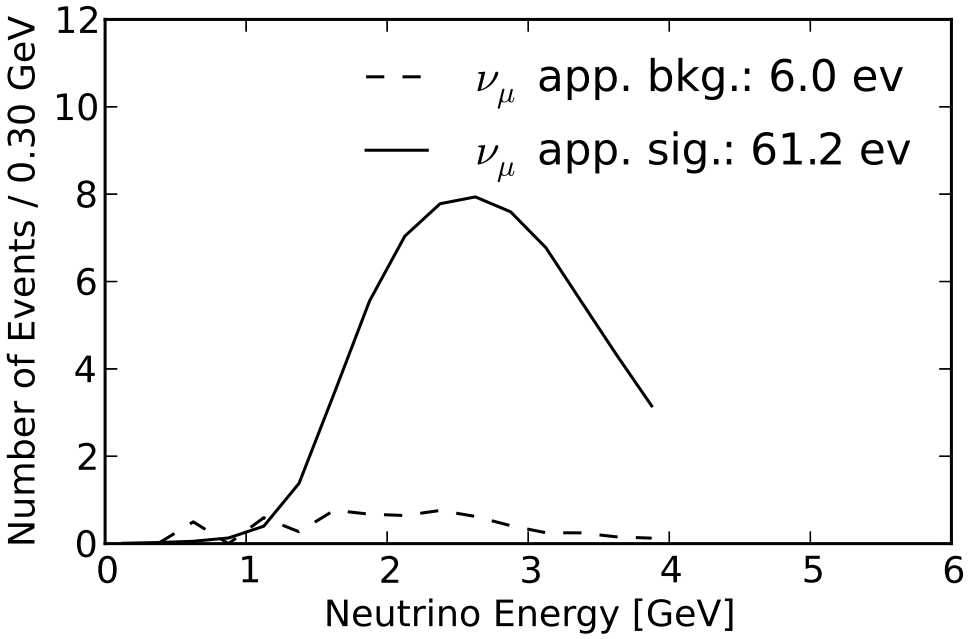

Figure 45. The expected energy spectrum of signal and background events for stored positive muons. The energy smearing matrix described in the detector performance section is used. The fluctuations in the background correspond to fluctuations in the MC-derived matrices.

Sensitivity contours are shown in Fig. 46. For this figure, 10σ corresponds to the χ^2 value corresponding to the same p-value as a 10σ upward Gaussian fluctuation. This contour shows that in this channel alone νSTORM is able to provide an 10σ measurement of the LSND anomaly. A near detector is not required for the appearance physics analysis, unlike that of the disappearance analysis, given the accelerator instrumentation within the decay ring and that this channel is not systematically limited, thus much higher Δm^2 can be probed than at previous experiments. The momentum of 3.8 GeV/c and baseline of 2000 meters were chosen after an optimization (Shown in Fig. 47. The number of stored muons is independent of ring energy since the 10% relative acceptance of the ring increases absolutely with energy and counteracts the decrease of pion production at higher energies (Fig. 5, right).

a. Optimizations

As the cuts-based detector performance section improves and various cost optimizations are done, there are numerous parameters that can be optimized to compensate and conserve the physics that can be done with this facility. For example, the optimization of baseline and energy (Fig. 47) allows one to optimize the baseline depending on site constraints or vary the energy of the ring if the decay ring cost become excessive. As the cuts-based detector performance improves, the various background rejections (Fig. 48 and 49) allow for further overall optimizations with respect to physics reach. The tools have been developed that will allow us to optimize over all components of νSTORM.

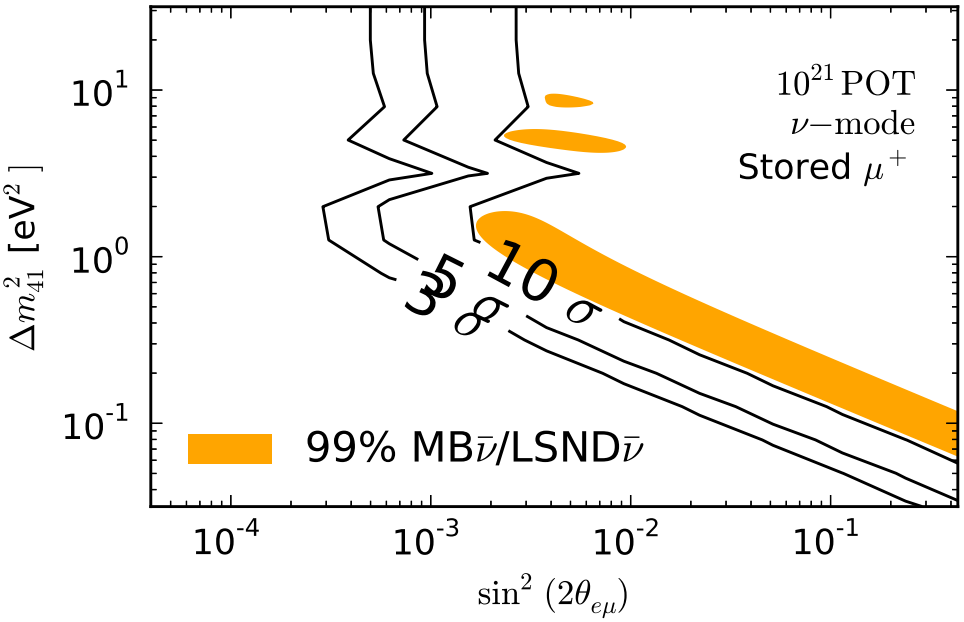

Figure 46. Contour in sterile parameter space associated with $\nu_e \to \nu_\mu$ appearance. Assumed is 1.8×10^{18} stored μ^+ at $p = (3.8\pm0.38)$ GeV/c and a detector at 2 kilometers with a fidicual mass of 1.3 kilotonne. A smearing matrix is used corresponding to 2 cm steel plates. The 150 m integration straight and detector volume are integrated over. The CPT-conjugate of the LSND best-fit region is shown.

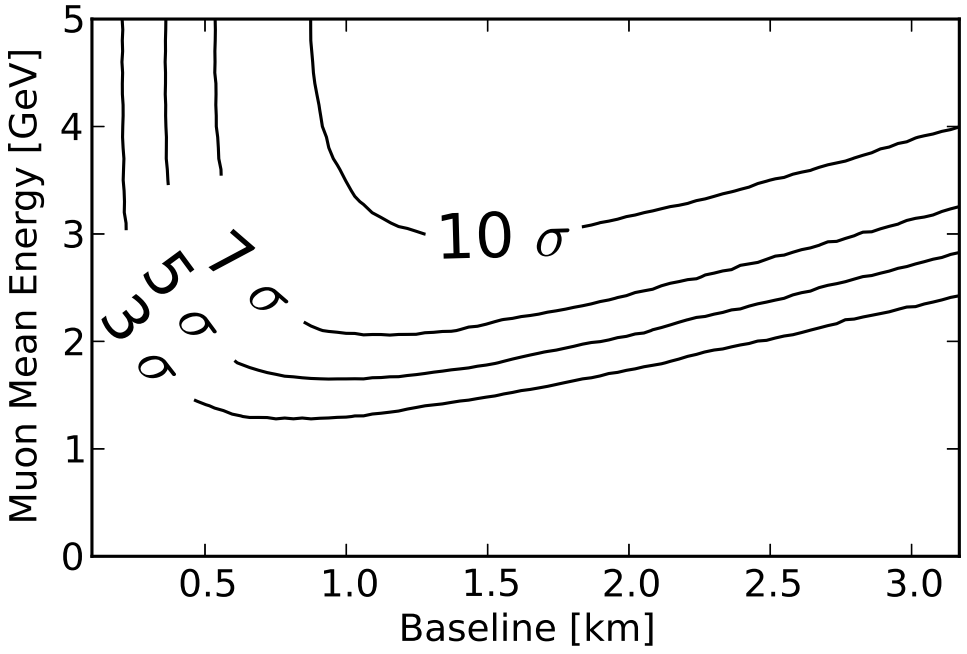

Figure 47. A baseline optimization using a total rates statistics-only χ^2, a signal efficiency of 0.5, and background rejection of charge misidentification and NCs at 10^{-3} and 10^{-4}.

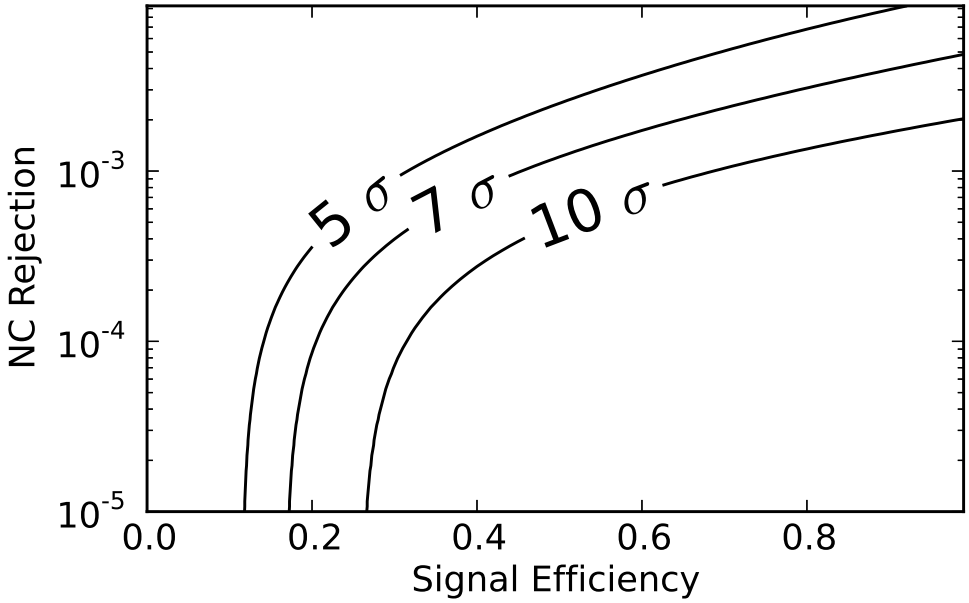

Figure 48. Tuning the NC rejection cut. The NC rejection level is shown versus the signal efficiency. A charge misidentification background of 10^{-4} is shown to illustrate when NC backgrounds become statistically significant. A total rates statistics-only χ^2 is used.

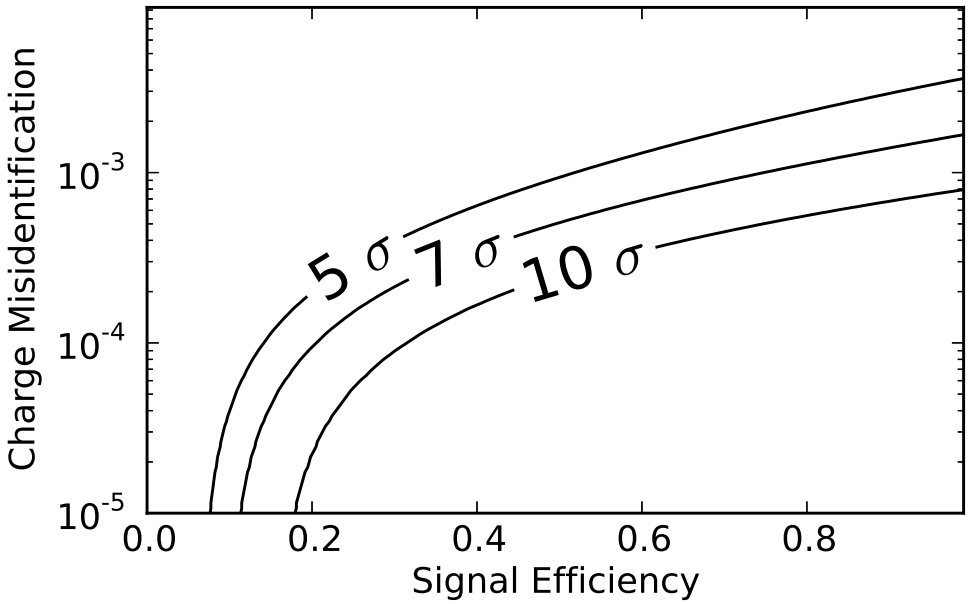

Figure 49. Tuning the charge misidentification cut. The charge misidentification level is shown versus the signal efficiency. A NC background of 10^{-4} is shown to illustrate when charge misidentification backgrounds become statistically significant. A total rates statistics-only χ^2 is used.

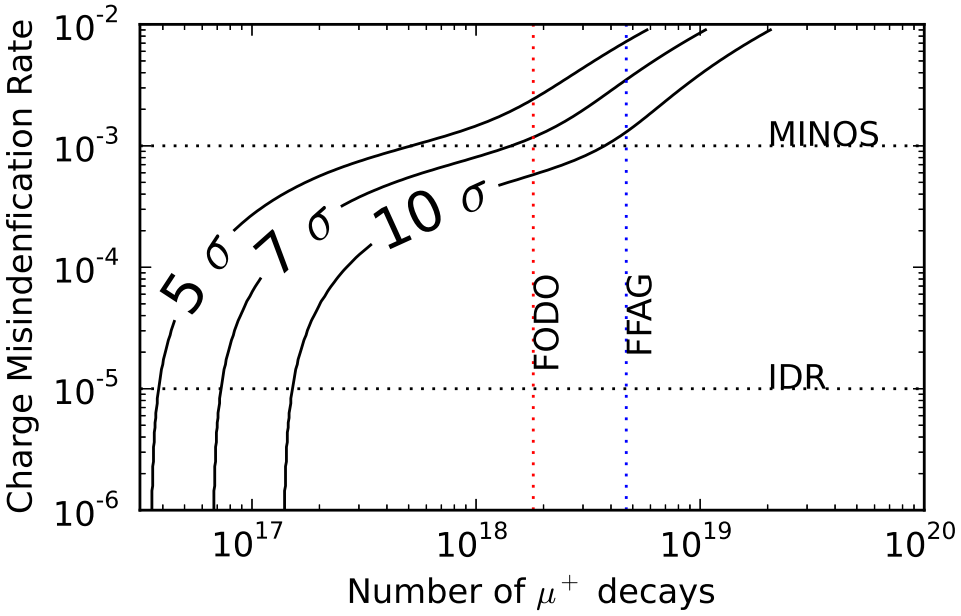

Figure 50. An optimization between the detector performance and accelerator performance using the charge misidentification rates and number of muon decays as the performance metric. IDR refers to the Interim Design Report [**?**] detector performance. FODO refers to the FODO lattice design that gives 1.8×10^{18} useful muon decays whilst FFAG refers to the FFAG design that gives 4.68×10^{18} useful muon decays. Both accelerators assume a front-end of the main injector at 60 GeV/c.

2. Disappearance channels

Since disappearance measurements are very sensitive to the signal normalization, additional near detectors have been proposed in $\bar{\nu}_e$ disappearance reactor experiments to measure θ_{13} [104, 105]. These near detectors are supposed to be as similar as possible to the far detectors, where the main purpose is to control the uncertainty on the reactor neutrino fluxes. This concept has been well established, and can be found in all of the state-of-the-art reactor experiments, such as Double Chooz, Daya Bay, and RENO. For νSTORM, the situation is very similar: while the flux is well under control, cross sections $\times$ efficiencies must be measured by a near detector. However, since oscillations may already take place in the near detector, the oscillation parameters need to be extracted in a self-consistent way in a combined near-far fit [106]. In fact, the near and far detectors may even swap the roles: while for $\Delta m^2 \simeq 1\,\mathrm{eV}^2$, the near detector effectively measures the cross sections and the far detector the oscillation, for $\Delta m^2 \gg 10\,\mathrm{eV}^2$, the near detector measures the oscillations and the far detector (where the oscillations average out) the cross sections.

For the near-far detector combination, there are two crucial issues: the systematics implementation and the treatment of geometry effects. In order to account for the uncertain cross sections $\times$ efficiencies, one can introduce a large systematic error, which is, however, fully correlated between the two detectors which measure the same flavors and polarities in the

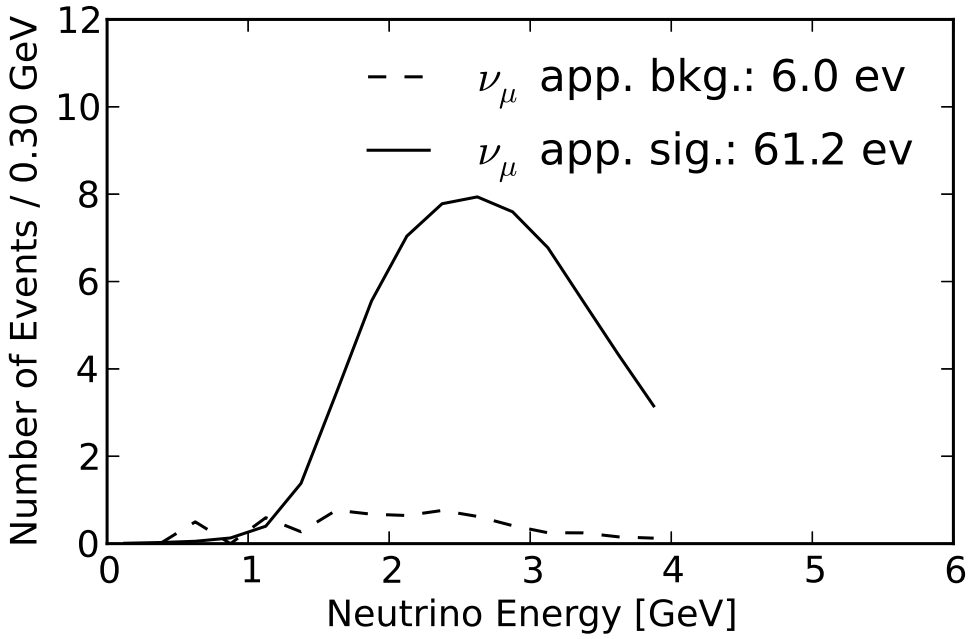

Figure 51. The expected energy spectrum of signal and background events for stored positive muons. The energy smearing matrix described in the detector performance section is used. The fluctuations in the background correspond to fluctuations in the MC-derived matrices.

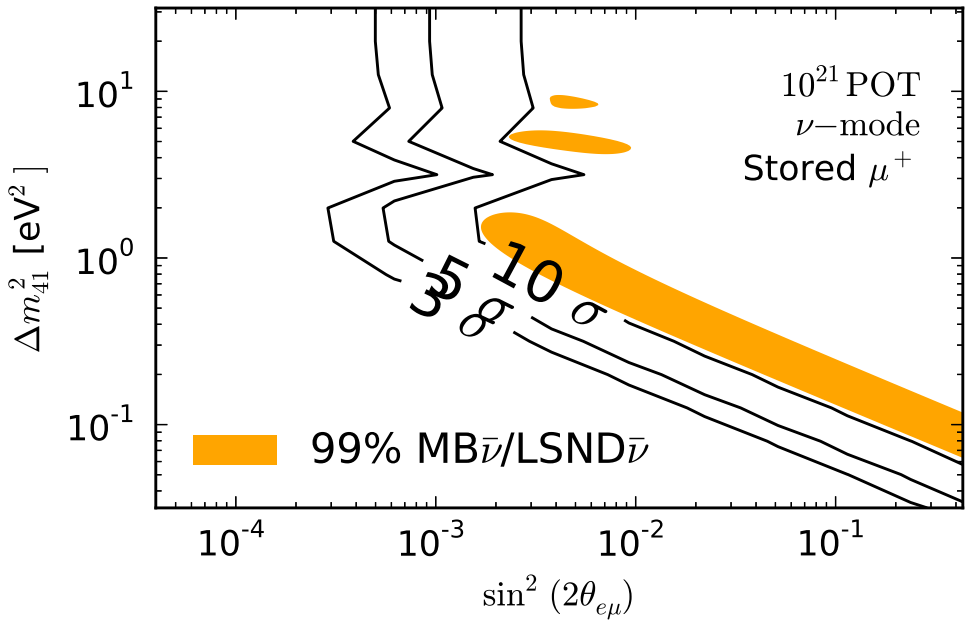

Figure 52. Contour in sterile parameter space associated with $\nu_e \to \nu_\mu$ appearance. Assumed is 1.8×10^{18} stored μ^+ at $p = (3.8\pm0.38)$ GeV/c and a detector at 2 kilometers with a fidicual mass of 1.3 kilotonne. A smearing matrix is used corresponding to 2 cm steel plates. The 150 m integration straight and detector volume are integrated over. The CPT-conjugate of the LSND best-fit region is shown [**?**].

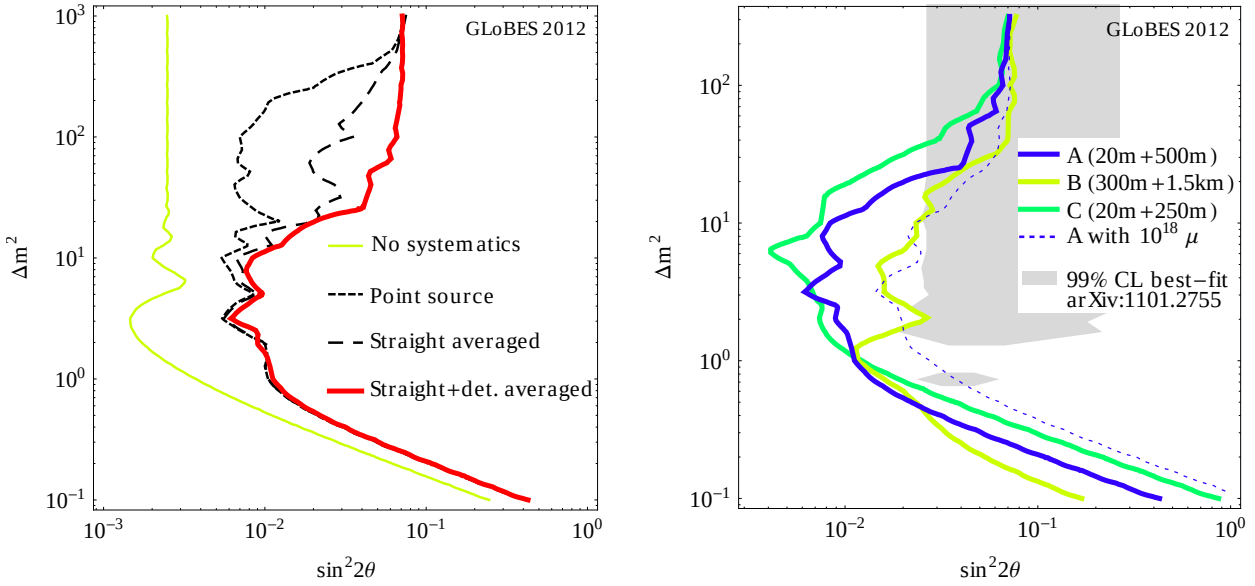

Figure 53. Exclusion region in $\sin^2 2\theta$-Δm^2 (right hand sides of curves) for ν_e disappearance for different geometry assumptions (left panel) and optimization points (right panel); 90% CL, 2 d.o.f. Left panel: The curve "no systematics" represents a single detector at $d = 500\,\mathrm{m}$ using statistics only, whereas the other curves correspond to near-far detector setups, where the red thick curves include (conservative) full systematics, including a 10% shape error, and geometry effects. Right panel: Systematics are fully included, different two-distance optimization points shown (distances to the end of the decay straight). Both panels: $E_\mu = 2\,\mathrm{GeV}$, 10^{19} useful muon decays per polarity, $d_1 = 20\,\mathrm{m}$ (200 t) and $d_2 = 500\,\mathrm{m}$ (1 kt), unless noted otherwise. Note that the curve labeled disappearance in Fig. II C has to be compared to the *product* of the ν_e and ν_μ disappearance sensitivities. Figure taken from Ref. [103].

disappearance channels. We adopt the most conservative case for this systematic: we even assume a completely unknown shape, i.e., we assume that the cross sections × efficiencies are unknown to the level of 10% within each bin, uncorrelated among the bins, but fully correlated between the near and far detectors (shape error); for details and further considered systematics see Ref. [103]. Especially for the near detector, geometry effects turn out to be important: the oscillations will average over the finite decay straight [103, 106], and the beam divergence, which cannot be avoided at least from the muon decay kinematics, will lead to a different beam spectrum in the near and far detectors [103, 107]. These effects are illustrated in Fig. 53, left panel, in the two flavor picture: The curve "Point source" shows the sensitivity assuming a point neutrino source and a near detector in the far distance limit, including full systematics. In this curve, a double peak in terms of Δm^2 can be clearly seen, coming from the oscillations taking place in the near ($\Delta m^2 \gg 10\,\mathrm{eV}^2$) or far ($\Delta m^2 \simeq 1\,\mathrm{eV}^2$) detector. If, however, the averaging over the decay straight ("Straight averaged") and the detector geometry ("Straight+detector averaged") are taken into account, the large ($\Delta m^2 \gg 10\,\mathrm{eV}^2$) sensitivity vanishes. The $\sin^2 2\theta$ reach for very large Δm^2 relies

on the external knowledge of systematics, in this case it is limited by the 10% shape error

As far as the two-baseline optimization is concerned [103], the optimal choice depends somewhat on the value of Δm^2. This is illustrated in the right panel of Fig. 53, where the sensitivities for several optimization points are shown. While all of these options perform equally well for $\Delta m^2 \simeq 1\,\mathrm{eV}^2$, larger values of $\Delta m^2 \simeq 1\,\mathrm{eV}^2$ prefer shorter distances (from the end of the decay straight) for the far detector. The optimization point A (20 m+500 m) seems to be a good compromise between the small and large Δm^2 sensitivities for $E_\mu = 2\,\mathrm{GeV}$. This is consistent with the optimization for appearance, but somewhat on the lower end of the optimal baseline range for that. For larger E_μ, slightly longer far detector distances are preferred, which means that 500 m to 800 m seems a reasonable distance range. For the near detector, we find that, in spite of the geometry effects, as short as possible distances are preferred if the far detector is in that baseline range.

As for the absolute performance, we show in Fig. 53 (right panel) the 99% CL best-fit from one of the global (anomaly) fits in the literature for comparison. It is clear that νSTORM can exclude this region for all of the optimization points for $\Delta m^2 \lesssim 10\,\mathrm{eV}^2$. However, note that either significantly more than 10^{18} useful muon decays per polarity (dashed curve) are needed for that purpose, or muon energies slightly higher than 2 GeV, as it the case in this document as the central momentum under consideration is 3.8 GeV/c. It can be shown that the proposed setup then has excellent sensitivity to both ν_e and ν_μ disappearance, both for neutrinos and antineutrinos [103], where the details somewhat depend on the final exposure, detection efficiency, and systematics treatment.

VII. OUTLOOK AND CONCLUSIONS

The physics case for experiments that search for sterile neutrinos is compelling. Beyond the hints from LSND, MiniBooNE and the reactor $\bar{\nu}_e$ flux anomaly, sterile neutrinos arise naturally in many extensions of the Standard Model. They appear in GUT models, in the seesaw mechanism and may also have an impact in cosmology as they are a possible candidate for DM or hot DM. Of the 30 or so ideas to search for sterile neutrinos that have recently been discussed in the literature, νSTORM is the only one that can do all of the following:

- Make a direct test of the LSND and MiniBooNE anomalies.
- Provide stringent constraints for both ν_e and ν_μ disappearance to over constrain $3+N$ oscillation models and to test the Gallium and reactor anomalies directly.
- Test the CP- and T-conjugated channels as well, in order to obtain the relevant clues for the underlying physics model, such as CP violation in $3+2$ models.

We have demonstrated the wide range of science that νSTORM can deliver, ranging from probing the existence (or non-existence) of sterile neutrinos to neutrino interaction physics in support of future programs, to the demonstration of and test-bed for novel accelerator technology. The 10 oscillation channels which νSTORM can probe allows for the study, in depth and in detail, of the various sterile oscillation scenarios that are theoretically motivated, while simultaneously being the only proposal that can directly test the LSND anomaly at 10 σ. A source of both electron and muon neutrinos allow for detailed cross section measurements where the electron neutrino cross section will be particularly important for future long baseline programs. Experimental R&D could also be done using this precisely understood neutrino source. The program that has been proposed is able to do relevant physics on both the short term and long term.

A. Proceeding toward a full Proposal

In order to present a full proposal to the laboratory (with a defensible cost estimate), additional scientific and engineering effort will be required. We have estimated this effort and itemize it in Table X.

Table X. Estimated effort to produce full proposal

Task	ΣFTE
Target Station	0.75
Capture & transport	1.25
Injection	0.25
Decay ring	2
Far Detector (Engineering)	1
Far Detector (Sim & Analysis)	2
Near Detector (Engineering)	1
Near Detector (Sim & Analysis)[a]	3.5
Costing	1
Total	**11.25**

[a] Note:Much of this effort is in complete synergy with the work on-going for the LBNE near detectors. And what is given here is likely an overestimate for what will be needed for the νSTORM proposal.

Appendix A: Magnetized Totally Active Detector

We have shown in Sec. IV that a magnetized detector is required for νSTORM if we wish to study the $\overline{\nu}_\mu$ oscillation appearance channels and that this naturally lead to the choice of magnetized iron technology. If one wanted to also look for $\overline{\nu}_e$ appearance, then magnetized totally active detector technology would be an appropriate alternative. Magnetic solutions for totally active detectors were studied within the International Scoping Study (ISS) [108] in the context of investigating how very large magnetic volumes could be produced at an acceptable cost. A liquid Argon (LAr) or a totally-active sampling scintillator detector (TASD) could be placed inside such a volume giving a magnetized totally active detector. The following technologies were considered:

- Room Temperature Coils (Al or Cu)
- Conventional Superconducting Coils
- High Tc Superconducting Coils
- Low Temperature Non-Conventional Superconducting Coils

Within the ISS much larger detector masses were considered than the 1 kT neeed for νSTORM. However, we can consider using one of the 10 large solenoids (each 15 m diameter $\times$ 15 m long) studied in the ISS for use with a 1 kT LAr. The ISS concept of a "magnetic cavern" is shown in Fig. A.

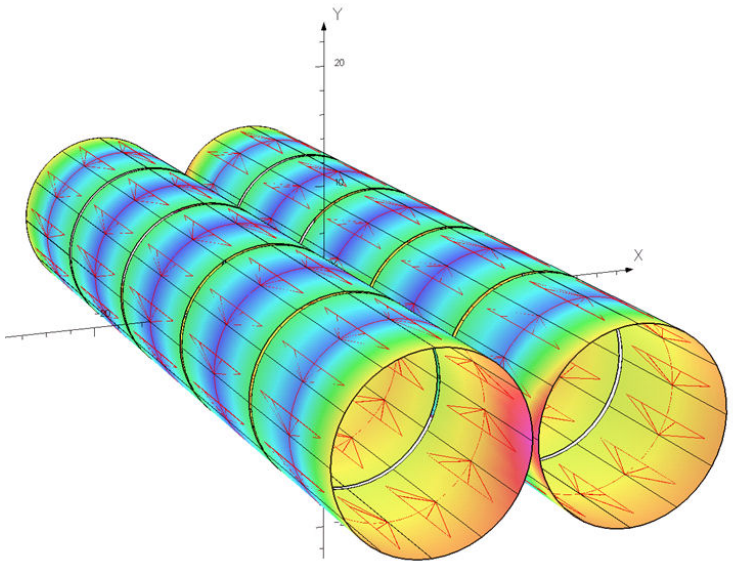

Figure 54. Magnetic Cavern Configuration

1. Conventional Room Temperature Magnets

In order to get adequate field strength with tolerable power dissipation, conventional room-temperature coils would have to be relatively thick. We first considered Al conductor operating at 150K. We then determined the amount of conductor necessary to produce a reference field of only 0.1T. In order to keep the current density at approximately 100A/cm^2, 10 layers of 1 cm^2 Al conductor would be required for our 15 m diameter $\times$ 15 m long reference solenoid. Using a \$20/kg cost for convention magnets [109], the estimated cost for 1 solenoid is \$5M. The power dissipation (assuming R=1 $\times$ 10$^-$8 Ohm-m is approximately 1 MW. The operating costs for 1 MW of power would be \$1.5M/year (based on typical US power costs). The cost of the magnet system including 10 years of operation is then \$20M. If one includes the cost of cooling the coils to 150K, the costs increase substantially. Studies have shown ([109] that there is little cost benefit to operating non-superconducting (Al or Cu) coils at low temperature vs. room temperature. If we consider that the power dissipation at room temperature for Al coils triples (vs. 150K operation), then the total magnet cost increases to \$50M.

2. Conventional Superconducting Coils

Conventional superconducting solenoids are certainly an option for providing the large magnetic volumes that are needed. Indeed coils of the size we are considering were engineered (but never built) for the proposed GEM experiment at the SSC. A cylindrical geometry (solenoid) does imply that a fraction of the magnetic volume will not be outside the volume of the active detector which will likely be rectangular in cross section. This is certainly a disadvantage in terms in the terms of efficient use of the magnetic volume, but would provide personnel access paths to detector components inside the magnetic cavern. It is certainly possible to consider solenoids of rectangular cross section and thus make more efficient use the magnetic volume, but the engineering and manufacturing implications of this type of design have not been evaluated.

Technically, superconducting magnets of this size could be built, but at what cost? There have been a number of approaches to estimating the cost of a superconducting magnet and we will mention two of those there. The first comes from Green and St. Lorant [110]. They looked at all the magnets that had been built at the time of their study (1993) and developed two formulas for extrapolating the cost of a superconducting magnet: one scaling by stored energy and one scaling by magnetic volume times field. They are given below:

$$C = 0.5(E_s)^{0.662} \tag{A1}$$

and

$$C = 0.4(BV)^{0.635} \tag{A2}$$

where E_s is the stored energy in MJ, B in the field in Tesla, V is the volume in m^3 and C is the cost in M\$. The formulas given above give a cost for each 15 m diameter × 15 m long, 0.5T magnet of approximately \$20M (based on E_s) and \$38M (based on magnetic volume). As another reference point, we used the CMS coil [111] (B=4T, V=340 m^3, Stored energy = 2.7 GJ, Cost = \$55M). The Green and St. Lorant formulas give costs for the CMS magnet of \$93M and \$41M based on stored energy and magnetic volume respectively. From these data we can make "Most Optimistic" and "Most Pessimistic" extrapolations for our baseline NF solenoid. The most optimistic cost comes from using the formula, based on stored energy and assume that it over-estimates by a factor of 1.7 (93/55) based on the CMS as built cost. This gives a cost of \$14M for each of our NF detector solenoids. The most pessimistic cost extrapolation comes from using the formula based on magnetic volume and conclude that it under-estimates the cost by a factor of 1.3 (55/41), based on the CMS as built cost. This then gives a cost of \$60M for each of our NF detector solenoids. There is obviously a large uncertainty represented here.

Another extrapolation model was used by Balbekov *et al.* [112] based on a model developed by A. Herve. The extrapolation formulae are given below:

$$P_0 = 0.33S^{0.8} \tag{A3}$$

$$P_E = 0.17E^{0.7} \tag{A4}$$

and

$$P = P_0 + P_E \tag{A5}$$

where P_0 is the price of the equivalent zero-energy magnet in MCHF, P_E is the price of magnetization, and P is the total price. S is the surface area (m^2) of the cryostat and E (MJ) is the stored energy. This model includes the cost of power supplies, cryogenics and vacuum plant. From the above equations you can see that the model does take into account the difficulties in dealing with size separately from magnetic field issues. Balbekov et. al. used three "as-builts" to derive the coefficients in the above equations:

- ALEPH (R=2.65m, L=7m, B=1.5T, E=138MJ, P=\$14M)
- CMS (R-3.2m, L=14.5m, B=4T, E=3GJ, P=\$55M)
- GEM (R=9m, L=27m, B=0.8T, E=2GJ, P=\$98M)

The GEM magnet cost was an estimate based on a detailed design and engineering analysis. Using this estimating model we have for one of the NF detector solenoids: $P_0 = 0.33(707)^{0.8}$ = 63MCHF, $P_E = 0.17(265)^{0.7}$ = 8.5MCHF. The magnet cost is thus approximately \$57M (which is close to our most pessimistic extrapolation given above). One thing that stands out is that the magnetization costs are small compared to the total cost. The mechanical costs involved with dealing with the large vacuum loading forces on the vacuum cryostat assumed to be used for this magnet are by far the dominant cost.

3. Low Temperature Non-Conventional Superconducting Coils

In this concept we solve the vacuum loading problem of the cryostat by using the superconducting transmission line (STL) that was developed for the Very Large Hadron Collider superferric magnets [77]. The solenoid windings now consist of this superconducting cable which is confined in its own cryostat. Each solenoid consists of 150 turns and requires 7500 m of cable. There is no large vacuum vessel and access to the detectors can be made through the winding support cylinder since the STL does not need to be close-packed in order to reach an acceptable field. We have performed a simulation of the Magnetic Cavern concept using STL solenoids and the results are shown in Fig. A 3. With the iron end-walls (1m thick), the average field in the XZ plane is approximately

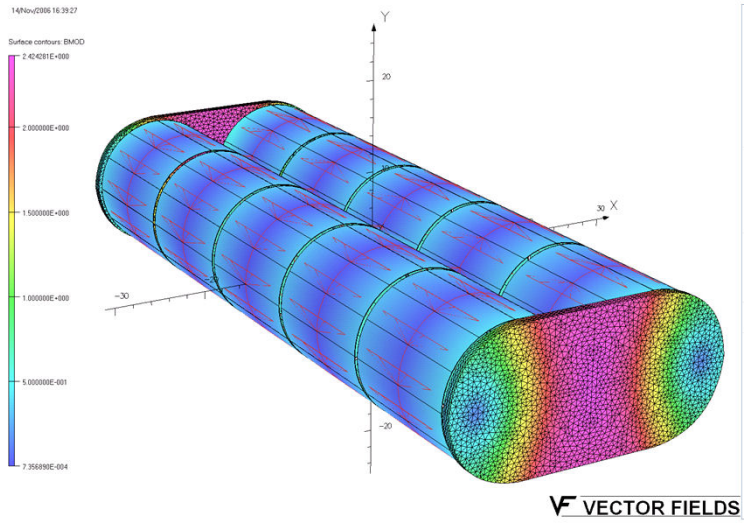

Figure 55. STL Solenoid Magnetic Cavern Simulation

0.58 T at an excitation current of 50 kA. The maximum radial force is approximately 16 kN/m and the maximum axial force approximately 40 kN/m. The field uniformity is quite good with the iron end-walls and is shown in Fig. A 3

4. Superconducting Transmission Line

The superconducting transmission line (STL) consists of a superconducting cable inside a cryopipe cooled by supercritical liquid helium at 4.5-6.0 K placed inside a co-axial cryostat. It consists of a perforated Invar tube, a copper stabilized superconducting cable, an Invar helium pipe, the cold pipe support system, a thermal shield covered by multilayer superinsulation, and the vacuum shell. One of the possible STL designs developed for the VLHC is shown in Fig. A 4.

The STL is designed to carry a current of 100 kA at 6.5 K in a magnetic field up to 1 T. This provides a 50% current margin with respect to the required current in order to reach a

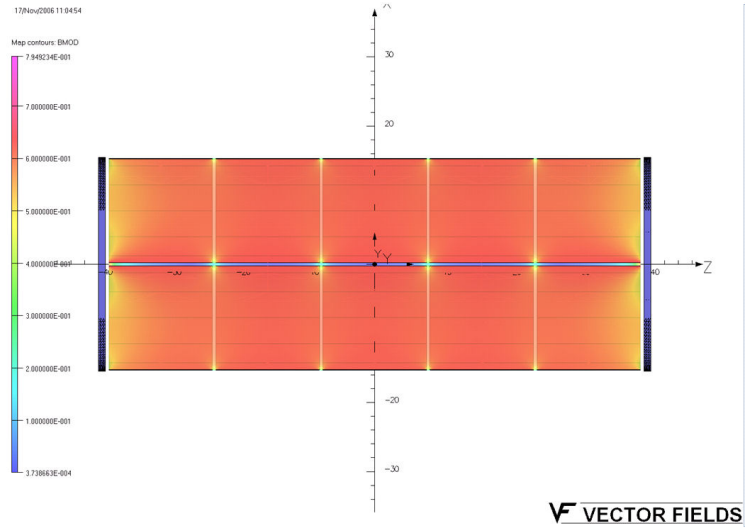

Figure 56. STL Solenoid Magnetic Cavern Field Uniformity in XZ plane

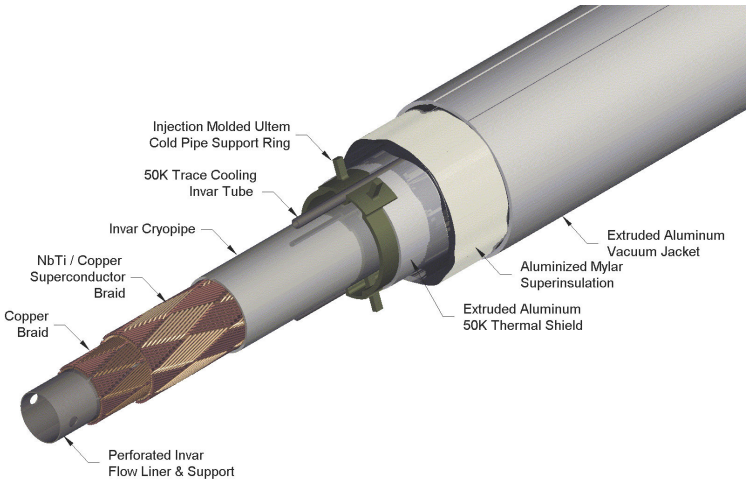

Figure 57. Superconducting transmission line

field of 0.5T. This operating margin can compensate for temperature variations, mechanical or other perturbations in the system. The superconductor for the STL could be made in the form of braid or in the form of a two-layer spiral winding using Rutherford cable. The braid consists of 288 NbTi SSC-type strands 0.648 mm in diameter and arranged in a pattern of two sets of 24 crossing bundles with opposite pitch angle about the tube. A conductor made of Rutherford cables consists of 9 NbTi cables that were used in the SSC dipole inner layer. A copper braid is placed inside the superconductor to provide additional current carrying capability during a quench. The conductor is sandwiched between an inner perforated Invar pipe, which serves as a liquid helium channel, and an outer Invar pressure pipe that closes the helium space. Both braided and spiral-wrapped conductors and the 10 cm long splice between them have been successfully tested with 100 kA transport current within the R&D program for the VLHC. The STL has a 2.5-cm clear bore which is sufficient for the liquid helium flow in a loop up to 10 km in length. This configuration allows for cooling each

solenoid with continuous helium flow coming from a helium distribution box.

The thermal shield is made of extruded aluminum pipe segments, which slide over opposite ends of each support spider. The 6.4-mm diameter Invar pipe is used for 50 K pressurized helium. It is placed in the cavities at the top and the bottom of both the shield and the supports. The shield is wrapped with 40 layers of a dimpled super insulation. The vacuum shell is made of extruded aluminum or stainless steel. Heat load estimates for the described STL are:

- Support system: 53 mW/m at 4.5 K and 670 mW/m at 40 K
- Super insulation: 15 mW/m at 4.5 K and 864 mW/m at 40K

The estimated cost of the described STL is approximately $500/m. Further STL design optimization will be required to adjust the structure to the fabrication and operating conditions of the desired detector solenoids and to optimize its fabrication and operational cost.

5. Conclusions

Magnetizing volumes large enough to contain upwards of 1kT of LAr or totally active scintillator at fields up to 0.5T with the use of the STL concept would appear to be possible, but would require dedicated R&D to extend the STL developed for the VLHC to this application. It eliminates the cost driver of large conventional superconducting coils, the vacuum-insulated cryostat, and has already been prototyped, tested, and costed during the R&D for the VLHC. A full engineering design would still need to be done, but this technique has the potential to deliver the large magnetic volume required with a field as high as 1T, with very uniform field quality and at an acceptable cost.

[1] D. G. Koshkarev, "Proposal for a Decay Ring to Produce Intense Secondary Particle Beams at the SPS," (1974), CERN/ISR-DI/74-62.

[2] D. Neuffer, "Design Considerations for a Muon Storage Ring," (1980), Telmark Conference on Neutrino Mass, Barger and Cline eds., Telmark, Wisconsin.

[3] S. Geer, Phys.Rev. **D57**, 6989 (1998), arXiv:hep-ph/9712290 [hep-ph].

[4] S. Choubey *et al.* (The IDS-NF collaboration), (2011), arXiv:1112.2853 [hep-ex].

[5] K. Abazajian, M. Acero, S. Agarwalla, A. Aguilar-Arevalo, C. Albright, *et al.*, (2012), arXiv:1204.5379 [hep-ph].

[6] M. Bando and K. Yoshioka, Prog.Theor.Phys. **100**, 1239 (1998), arXiv:hep-ph/9806400 [hep-ph].

[7] E. Ma, Phys.Lett. **B380**, 286 (1996), arXiv:hep-ph/9507348 [hep-ph].

[8] Q. Shafi and Z. Tavartkiladze, Phys.Lett. **B451**, 129 (1999), arXiv:hep-ph/9901243 [hep-ph].

[9] K. Babu and G. Seidl, Phys.Rev. **D70**, 113014 (2004), arXiv:hep-ph/0405197 [hep-ph].

[10] A. Kusenko, F. Takahashi, and T. T. Yanagida, Phys.Lett. **B693**, 144 (2010), arXiv:1006.1731 [hep-ph].

[11] R. Mohapatra, Phys.Rev. **D64**, 091301 (2001), arXiv:hep-ph/0107264 [hep-ph].

[12] C. Froggatt and H. B. Nielsen, Nucl.Phys. **B147**, 277 (1979).

[13] J. Barry, W. Rodejohann, and H. Zhang, JCAP **1201**, 052 (2012), arXiv:1110.6382 [hep-ph].

[14] R. Mohapatra, S. Nasri, and H.-B. Yu, Phys.Rev. **D72**, 033007 (2005), arXiv:hep-ph/0505021 [hep-ph].

[15] C. S. Fong, R. N. Mohapatra, and I. Sung, Phys.Lett. **B704**, 171 (2011), arXiv:1107.4086 [hep-ph].

[16] H. Zhang, (2011), arXiv:1110.6838 [hep-ph].

[17] Z. G. Berezhiani and R. N. Mohapatra, Phys.Rev. **D52**, 6607 (1995), arXiv:hep-ph/9505385 [hep-ph].

[18] R. Foot and R. Volkas, Phys.Rev. **D52**, 6595 (1995), arXiv:hep-ph/9505359 [hep-ph].

[19] V. Berezinsky, M. Narayan, and F. Vissani, Nucl.Phys. **B658**, 254 (2003), arXiv:hep-ph/0210204 [hep-ph].

[20] A. Aguilar *et al.* (LSND), Phys. Rev. **D64**, 112007 (2001), arXiv:hep-ex/0104049.

[21] A. Aguilar-Arevalo *et al.* (The MiniBooNE Collaboration), Phys.Rev.Lett. **98**, 231801 (2007), arXiv:0704.1500 [hep-ex].

[22] A. Aguilar-Arevalo *et al.* (The MiniBooNE Collaboration), Phys.Rev.Lett. **105**, 181801 (2010), arXiv:1007.1150 [hep-ex].

[23] T. Mueller, D. Lhuillier, M. Fallot, A. Letourneau, S. Cormon, *et al.*, Phys.Rev. **C83**, 054615 (2011), arXiv:1101.2663 [hep-ex].

[24] K. Schreckenbach, G. Colvin, W. Gelletly, and F. Von Feilitzsch, Phys.Lett. **B160**, 325 (1985).

[25] P. Huber, Phys.Rev. **C84**, 024617 (2011), arXiv:1106.0687 [hep-ph].

[26] G. Mention, M. Fechner, T. Lasserre, T. Mueller, D. Lhuillier, *et al.*, Phys.Rev. **D83**, 073006 (2011), arXiv:1101.2755 [hep-ex].

[27] P. Anselmann *et al.* (GALLEX Collaboration.), Phys.Lett. **B342**, 440 (1995).

[28] W. Hampel *et al.* (GALLEX Collaboration), Phys.Lett. **B420**, 114 (1998).

[29] J. Abdurashitov, V. Gavrin, S. Girin, V. Gorbachev, T. V. Ibragimova, *et al.*, Phys.Rev.Lett. **77**, 4708 (1996).

[30] J. Abdurashitov *et al.* (SAGE Collaboration), Phys.Rev. **C59**, 2246 (1999), arXiv:hep-ph/9803418 [hep-ph].

[31] J. Abdurashitov, V. Gavrin, S. Girin, V. Gorbachev, P. Gurkina, *et al.*, .

[32] M. A. Acero, C. Giunti, and M. Laveder, Phys.Rev. **D78**, 073009 (2008), arXiv:0711.4222 [hep-ph].

[33] C. Giunti and M. Laveder, Phys.Rev. **D82**, 053005 (2010), arXiv:1005.4599 [hep-ph].

[34] C. Giunti and M. Laveder, Phys.Rev. **C83**, 065504 (2011), arXiv:1006.3244 [hep-ph].

[35] J. Kopp, M. Maltoni, and T. Schwetz, Phys.Rev.Lett. **107**, 091801 (2011), arXiv:1103.4570 [hep-ph].

[36] C. Giunti and M. Laveder, Phys.Lett. **B706**, 200 (2011), arXiv:1111.1069 [hep-ph].

[37] G. Karagiorgi, (2011), arXiv:1110.3735 [hep-ph].

[38] C. Giunti and M. Laveder, Phys.Rev. **D84**, 093006 (2011), arXiv:1109.4033 [hep-ph].

[39] C. Giunti and M. Laveder, Phys.Rev. **D84**, 073008 (2011), arXiv:1107.1452 [hep-ph].

[40] B. Armbruster *et al.* (KARMEN), Phys. Rev. **D65**, 112001 (2002), arXiv:hep-ex/0203021.

[41] P. Astier *et al.* (NOMAD), Nucl. Phys. **B611**, 3 (2001), arXiv:hep-ex/0106102.

[42] F. Dydak, G. Feldman, C. Guyot, J. Merlo, H. Meyer, *et al.*, Phys.Lett. **B134**, 281 (1984).

[43] Y. Ashie *et al.* (Super-Kamiokande), Phys. Rev. **D71**, 112005 (2005), hep-ex/0501064.

[44] P. Adamson *et al.* (The MINOS Collaboration), Phys.Rev. **D81**, 052004 (2010), arXiv:1001.0336 [hep-ex].

[45] P. Adamson *et al.* (MINOS Collaboration), Phys.Rev.Lett. **107**, 011892 (2011), arXiv:1104.3922 [hep-ex].

[46] Y. Declais, J. Favier, A. Metref, H. Pessard, B. Achkar, *et al.*, Nucl.Phys. **B434**, 503 (1995).

[47] Y. Declais, H. de Kerret, B. Lefievre, M. Obolensky, A. Etenko, *et al.*, Phys.Lett. **B338**, 383 (1994).

[48] A. Kuvshinnikov, L. Mikaelyan, S. Nikolaev, M. Skorokhvatov, and A. Etenko, JETP Lett. **54**, 253 (1991).

[49] G. Vidyakin, V. Vyrodov, I. Gurevich, Y. Kozlov, V. Martemyanov, *et al.*, Sov.Phys.JETP **66**, 243 (1987).

[50] H. Kwon, F. Boehm, A. Hahn, H. Henrikson, J. Vuilleumier, *et al.*, Phys.Rev. **D24**, 1097 (1981).

[51] G. Zacek *et al.* (CALTECH-SIN-TUM), Phys. Rev. **D34**, 2621 (1986).

[52] M. Apollonio *et al.* (CHOOZ), Eur. Phys. J. **C27**, 331 (2003), arXiv:hep-ex/0301017.

[53] F. Boehm, J. Busenitz, B. Cook, G. Gratta, H. Henrikson, *et al.*, Phys.Rev. **D64**, 112001 (2001), arXiv:hep-ex/0107009 [hep-ex].

[54] P. Huber, M. Lindner, and W. Winter, Comput. Phys. Commun. **167**, 195 (2005), arXiv:hep-ph/0407333.

[55] P. Huber, J. Kopp, M. Lindner, M. Rolinec, and W. Winter, Comput. Phys. Commun. **177**, 432 (2007), hep-ph/0701187.

[56] M. C. Gonzalez-Garcia and M. Maltoni, Phys. Rept. **460**, 1 (2008), arXiv:0704.1800 [hep-ph].

[57] M. Maltoni and T. Schwetz, Phys. Rev. **D76**, 093005 (2007), arXiv:0705.0107 [hep-ph].

[58] E. Akhmedov and T. Schwetz, JHEP **10**, 115 (2010), arXiv:1007.4171 [hep-ph].

[59] M. Maltoni and T. Schwetz, Phys. Rev. **D68**, 033020 (2003), arXiv:hep-ph/0304176.

[60] M. Gonzalez-Garcia, M. Maltoni, and J. Salvado, JHEP **08**, 117 (2010), arXiv:1006.3795 [hep-ph].

[61] J. Hamann, S. Hannestad, G. G. Raffelt, I. Tamborra, and Y. Y. Wong, Phys.Rev.Lett. **105**, 181301 (2010), arXiv:1006.5276 [hep-ph].

[62] E. Giusarma, M. Corsi, M. Archidiacono, R. de Putter, A. Melchiorri, *et al.*, Phys.Rev. **D83**, 115023 (2011), arXiv:1102.4774 [astro-ph.CO].

[63] G. Mangano and P. D. Serpico, Phys.Lett. **B701**, 296 (2011), arXiv:1103.1261 [astro-ph.CO].

[64] J. Hamann, S. Hannestad, G. G. Raffelt, and Y. Y. Wong, JCAP **1109**, 034 (2011), arXiv:1108.4136 [astro-ph.CO].

[65] L. Bento and Z. Berezhiani, Phys.Rev. **D64**, 115015 (2001), arXiv:hep-ph/0108064 [hep-ph].

[66] A. Dolgov and F. Takahashi, Nucl.Phys. **B688**, 189 (2004), arXiv:hep-ph/0402066 [hep-ph].

[67] G. Karagiorgi, M. Shaevitz, and J. Conrad, (2012), arXiv:1202.1024 [hep-ph].

[68] J. Hewett, H. Weerts, R. Brock, J. Butler, B. Casey, *et al.*, (2012), arXiv:1205.2671 [hep-ex].

[69] P. Huber, M. Mezzetto, and T. Schwetz, JHEP **0803**, 021 (2008), arXiv:0711.2950 [hep-ph].

[70] P. Coloma, A. Donini, E. Fernandez-Martinez, and P. Hernandez, (2012), 30 pages, 9 figures, arXiv:1203.5651 [hep-ph].

[71] J. Formaggio and G. Zeller, "From eV to EeV: Neutrino Cross Sections Across Energy Scales," (2012), to be published in Rev. Mod. Phys.

[72] D. Casper, Nucl.Phys.Proc.Suppl. **112**, 161 (2002), to be published in Proceedings of the First International Workshop on Neutrino-Nucleus Interactions in the Few-GeV Region (NUINT'01), arXiv:hep-ph/0208030 [hep-ph].

[73] N. Mokhov, J.Nucl.Sci.Tech. **S1**, 167 (2000).

[74] N. Bozhko *et al.*, Yad. Fiz **31**, 1494.

[75] L. Barkov *et al.*, Sov. J. Nucl. Phys. **35(5)**, 694.

[76] D. G. Michael *et al.* (MINOS), Nucl. Instrum. Meth. **A596**, 190 (2008), arXiv:0805.3170 [physics.ins-det].

[77] G. Ambrosio *et al.* (VLHC Design Study Group), (2001).

[78] R. Smith *et al.* (USCMS Collaboration), IEEE Trans.Appl.Supercond. **14**, 1830 (2004).

[79] H. Maesaka (K2K SciBar Collaboration), , 185 (2003).

[80] Y. Kudenko (T2K), Nucl. Instrum. Meth. **A598**, 289 (2009), arXiv:0805.0411 [physics.ins-det].

[81] D. Greiner, T. Lachenmaier, J. Jochum, and A. Cabrera, Nucl. Instrum. Meth. **A581**, 139 (2007).

[82] Z. Sadygov, (1996), russian patent No. 2102820.

[83] N. Bacchetta *et al.*, Nucl. Instrum. Meth. **A383**, 263 (1996).

[84] D. Renker, Nucl.Instrum.Meth. **A598**, 207 (2009).

[85] B. Dolgoshein (SIPM Collaboration), , 442 (2003).

[86] K. Bechtol, S. Funk, A. Okumura, L. Ruckman, A. Simons, *et al.*, submitted to Nuclear Instrumentation and Methods (NIM) (2011), arXiv:1105.1832 [astro-ph.IM].

[87] S. R. Mishra, Prog.Part.Nucl.Phys. **64**, 202 (2010).

[88] J. Altegoer *et al.* (NOMAD Collaboration), Nucl.Instrum.Meth. **A404**, 96 (1998).

[89] T. Akesson *et al.* (ATLAS TRT Collaboration), Nucl.Instrum.Meth. **A522**, 131 (2004).

[90] V. Bychkov, M. Faessler, R. Geyer, N. Gorbacheva, Y. Gusakov, *et al.*, Part.Nucl.Lett. **111**, 64 (2002).

[91] C. Andreopoulos *et al.*, Nucl. Instrum. Meth. **A614**, 87 (2010), arXiv:0905.2517 [hep-ph].

[92] J. Apostolakis and D. H. Wright (Geant4), AIP Conf. Proc. **896**, 1 (2007).

[93] "Geant4 Physics Reference Manual," http://geant4.cern.ch/geant4/UserDocumentation/UsersGuides/PhysicsReferenceManual/html/.

[94] A. Pla-Dalmau, A. D. Bross, V. V. Rykalin, and B. M. Wood (MINERvA), "Extruded plastic scintillator for MINERvA," (2005), proceedings of 2005 IEEE Nuclear Science Symposium and Medical Imaging Conference, El Conquistador Resort, Puerto Rico, 23-29 Oct 2005.

[95] A. Cervera, A. Laing, J. Martin-Albo, and F. J. P. Soler, Nucl. Instrum. Meth. **A624**, 601 (2010), arXiv:1004.0358 [hep-ex].

[96] A. Laing, PhD thesis, University of Glasgow (2010).

[97] A. Cervera-Villanueva, J. J. Gomez-Cadenas, and J. A. Hernando, Nucl. Instrum. Meth. **A534**, 180 (2004).

[98] D. Emeliyanov, I. Gorbounov, and I. Kisel, "OTR/ITR-CATS: Tracking Based on Cellular Automaton and Kalman Filter," (2001), HERA-B note 01-137.

[99] D. Groom, N. Mokhov, and S. Striganov, Atomic Data and Nuclear Data Tables **78**, 183 (2001).

[100] P. Adamson *et al.*, Nucl. Instrum. Meth. **A556**, 119 (2006).

[101] G. Bari *et al.*, Nucl. Instrum. Meth. **A508**, 170 (2003).

[102] A. Blondel, M. Campanelli, and M. Fechner, Nucl. Instrum. Meth. **A535**, 665 (2004).

[103] W. Winter, (2012), arXiv:1204.2671 [hep-ph].

[104] H. Minakata, H. Sugiyama, O. Yasuda, K. Inoue, and F. Suekane, Phys.Rev. **D70**, 059901 (2004), arXiv:hep-ph/0211111 [hep-ph].

[105] P. Huber, M. Lindner, T. Schwetz, and W. Winter, Nucl.Phys. **B665**, 487 (2003), arXiv:hep-ph/0303232 [hep-ph].

[106] C. Giunti, M. Laveder, and W. Winter, Phys.Rev. **D80**, 073005 (2009), arXiv:0907.5487 [hep-ph].

[107] J. Tang and W. Winter, Phys.Rev. **D80**, 053001 (2009), arXiv:0903.3039 [hep-ph].

[108] T. Abe *et al.* (ISS Detector Working Group), JINST **4**, T05001 (2009), detector report of the International Scoping Study of a future Neutrino Factory and Super-Beam facility, 86 pages, 49 figures, arXiv:0712.4129 [physics.ins-det].

[109] M. Green, "Private communication,".
[110] M. Green and S. St. Lorant, Adv.Cryog.Eng. **39A**, 271 (1994).
[111] A. Herve, G. Acquistapace, D. Campi, P. Cannarsa, P. Fabbricatore, *et al.*, IEEE Trans.Appl.Supercond. **12**, 385 (2002).
[112] B. *et al.*, "MuCool Note 216," (2001).